

REVIEW

Open Access



A review of the mathematical modeling of equilibrium and nonequilibrium hypersonic flows

Wenqing Zhang, Zhijun Zhang^{*}, Xiaowei Wang and Tianyi Su

^{*}Correspondence:
zhjzhang@mail.neu.edu.cn

School of Mechanical
Engineering and Automation,
Northeastern University,
Shenyang 110819, China

Abstract

This paper systematically reviews the mathematical modeling based on the computational fluid dynamics (CFD) method of equilibrium and nonequilibrium hypersonic flows. First, some physicochemical phenomena in hypersonic flows (e.g., vibrational energy excitation and chemical reactions) and the flow characteristics at various altitudes (e.g., thermochemical equilibrium, chemical nonequilibrium, and thermochemical nonequilibrium) are reviewed. Second, the judgment rules of whether the CFD method can be applied to hypersonic flows are summarized for accurate numerical calculations. This study focuses on the related numerical models and calculation processes of the CFD method in a thermochemical equilibrium flow and two nonequilibrium flows. For the thermochemical equilibrium flow, the governing equations, chemical composition calculation methods, and related research on the thermodynamic and transport properties of air are reviewed. For the nonequilibrium flows, the governing equations that include one-, two-, and three-temperature models are reviewed. The one-temperature model is applied to a chemical nonequilibrium flow, whereas the two- and three-temperature models are applied to a thermochemical nonequilibrium flow. The associated calculations and numerical models of the thermodynamic and transport properties, chemical reaction sources, and energy transfers between different energy modes of the three models are presented in detail. Finally, the corresponding numerical models of two special wall boundary conditions commonly used in hypersonic flows (i.e., slip boundary conditions and catalytic walls) and related research, are reviewed.

Keywords: Mathematical modeling, Hypersonic flows, Chemical nonequilibrium flow, Thermochemical nonequilibrium flow, Thermochemical equilibrium flow

1 Introduction

Hypersonic vehicles, such as missiles, re-entry bodies, launch vehicles, and deep space detectors, have become the primary tools for strategic strikes, missile defense, space shuttles, and space exploration [1, 2]. Their extremely high speeds provide not only quick reach and responsiveness, but also temperatures that are sufficiently high to excite the internal vibrational energy within molecules and induce a series of chemical reactions (dissociation, exchange and even ionization) in the gas [3, 4]. These physicochemical

phenomena cause the properties of gas around hypersonic vehicles to disobey the “calorically perfect gas” [5]; for instance, the specific heats become functions of the temperature rather than constants. Moreover, considering the trajectories of hypersonic vehicles, the gas around vehicles always exhibits different characteristics at various altitudes [6]. The nonequilibrium phenomena occur when hypersonic vehicles fly at high altitudes.

These complex physicochemical phenomena and gas characteristics occurring at various altitudes significantly increase the difficulty of describing and solving hypersonic flow problems. Although particle methods [7], such as the Direct Simulation Monte Carlo (DSMC) method, can unify these phenomena and characteristics of hypersonic flows in a Boltzmann equation, the extreme computational effort prevents their application to large geometries and low altitudes [8].

To date, the computational fluid dynamics (CFD) method remains the primary numerical simulation method for modeling hypersonic flows at lower altitudes within continuum and near-continuum regimes owing to its high computational efficiency [9, 10]. To accurately describe these phenomena and characteristics by the CFD method, hypersonic flows can be classified into three types: thermochemical equilibrium, chemical nonequilibrium, and thermochemical nonequilibrium flows. For the thermochemical equilibrium flow, conventional Navier–Stokes (N-S) equations can be adopted, in which a single temperature is applied without coupling with the chemical reactions. For the nonequilibrium flow, three types of nonequilibrium N-S equations are applied to describe the corresponding nonequilibrium characteristics: the one-temperature model [11] for the chemical nonequilibrium flow, and the two- [12], and three-temperature models [13] for the thermochemical nonequilibrium flow.

Although the forms of these master equations are not complex, there are some challenges in their solution process, such as the accurate description of gas properties at high temperatures, chemical reaction processes, and energy transfers between various energy modes [14]. Since the 1950s, researchers have proposed many corresponding numerical models. However, understanding the derivation processes of these numerical models requires knowledge of statistical thermodynamics, kinetic theory, chemical kinetic methods, and even quantum mechanics, which can discourage readers from learning about the application of the CFD method in hypersonic flows.

The appropriate wall boundary conditions are vital to accurately predict the aerodynamic performance of hypersonic vehicles. Typically, two special wall boundary conditions are considered in hypersonic flows: slip boundary conditions and a catalytic wall. Recently, the effect of a catalytic wall on the prediction of the aerodynamic heat has become a research hotspot.

This paper introduces where and how CFD methods can be applied in hypersonic flows. It reviews two calculation processes and related numerical models of the CFD method for equilibrium and nonequilibrium flows, and two special wall boundary conditions. The purpose is to enable readers interested in hypersonic flows to systematically and quickly understand the numerical calculation process of the CFD method in this field. This paper is organized as follows. Section 2 introduces the physicochemical phenomena and characteristics of the hypersonic air flow at various altitudes. Section 3 summarizes the rules for determining the applicability of the CFD method in hypersonic flows. Section 4 summarizes the calculation process of the CFD method in the

thermochemical equilibrium flow, numerical models of the chemical composition, and related studies on the thermodynamic and transport properties of hypersonic air flows. Section 5 summarizes the numerical calculation process of the CFD method in nonequilibrium flows, and reviews various numerical models of the chemical reactions, thermodynamic and transport properties, and energy transfers since the nineteenth century. Finally, Section 6 highlights the wall boundary conditions, including the slip boundary conditions and catalytic walls, and reviews related numerical models and applications.

2 Characteristics of hypersonic flows

Hypersonic flows are always accompanied by a series of physicochemical phenomena, including vibrational energy excitation and chemical reactions [15]. Figure 1 shows the temperature ranges of the vibrational excitation and some chemical reactions of air derived from [3] along with the chemical reactions of air reviewed by Park [16]. As seen in Fig. 1, the vibrational energy of the molecules is excited when the temperature exceeds 800 K. The O₂ dissociation begins at 2500 K and ends at 4000 K, while the N₂ dissociation starts at 4000 K and ends at 9000 K. The exchange reactions involving NO occur at 2500–9000 K. As the temperature further increases, ionization reactions begin to occur; for example, N and O are ionized into N⁺, O⁺, and e⁻. There are some reactions that are not included in Fig. 1, such as associative ionization, exchange ionization, electron-impact ionization, and charge exchange reactions, which are listed in Table 2.

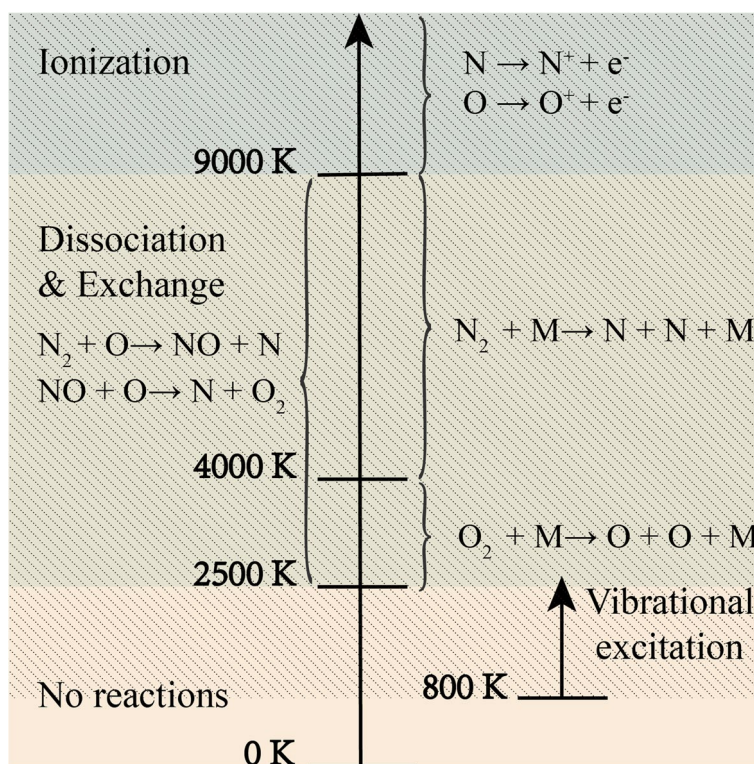


Fig. 1 Temperature ranges of vibrational excitation and chemical reactions of air

Taking the Apollo reentry as an example, the gas around the vehicle exhibits different characteristics at various altitudes, as shown in Fig. 2 [17, 18]. During reentry into the atmosphere, the vehicle traverses different flow regimes, from the free-molecular regime down to the continuum regime. According to the altitude and flight speed, the flow around the vehicle can be classified into three types: thermochemical nonequilibrium flow, chemical nonequilibrium flow, and thermochemical equilibrium flow. Nonequilibrium flow occurs when the gas flow is at a low density and/or involves very small length scales [19]. At high altitudes, owing to the rarefied gas environment, the number of intermolecular collisions is insufficient to achieve a new equilibrium state [20]. Under this condition, the relaxation process of chemical reactions and/or energy transfers between different energy modes must be considered. When the flow is in both chemical and thermal nonequilibrium, it is referred to as a thermochemical nonequilibrium flow. When the flow is in thermal equilibrium but in chemical nonequilibrium, it is referred to as a chemical nonequilibrium flow. At a low altitude, the sufficient number of collisions because of the high density maintains the gas in the well-known equilibrium state. All internal energy modes equilibrate with each other, and the chemical reactions have been fully carried out. This flow around the vehicle is called a thermochemical equilibrium flow.

3 Applicability judgment rules of the CFD method

The Knudsen number Kn , which gauges the degree of rarefaction of a gas [21], is used to divide the flow regime. It is expressed as

$$Kn = \lambda/L, \tag{1}$$

where λ is the local mean free path and L is the characteristic flow length.

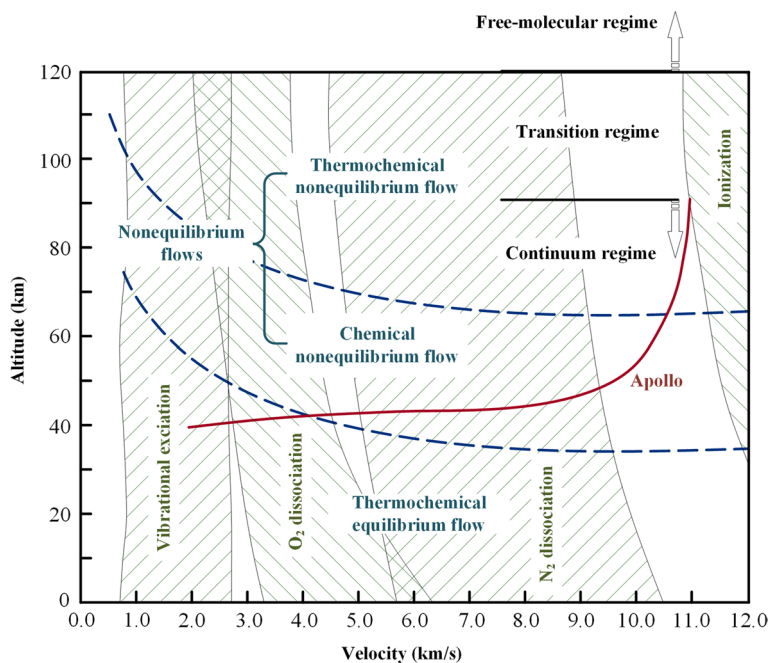


Fig. 2 Characteristics of hypersonic flows [17, 18]

There are four commonly accepted flow regimes [8, 22], as shown in Fig. 3.

- (1) Continuum flow, $Kn < 0.001$. The flow is considered to be continuous.
- (2) Slip flow, $0.001 < Kn < 0.1$. The flow velocity has a slightly tangential component at the boundaries of the surface of the body [23], and the transitional nonequilibrium is important near the surfaces.
- (3) Transitional flow, $0.1 < Kn < 10$. Insufficient intermolecular collisions cause the flow to depart from thermal equilibrium.
- (4) Free-molecular flow, $Kn > 10$. The intermolecular collisions can be neglected, and the gas only interacts with the walls of the object.

The Kn defined in Eq. (1) is applied to monatomic gases only considering the translational motion of gas molecules. However, for diatomic gases, there are also rotational and vibrational motions. Different relaxation times are required for these various motions to achieve a new equilibrium state, which easily results in the nonequilibrium phenomenon in the rarefied gas and high speeds. In rarefied gas dynamics, the temporal Knudsen number $Kn_{temporal}$ characterizes the rarefaction of various motions of the gas. It is expressed as

$$Kn_{temporal} \propto Kn \frac{\tau_i}{\tau_f}, \tag{2}$$

where τ_i represents the relaxation times of the chemical reactions and various internal energies (e.g., translational, rotational, and vibrational energies), and τ_f represents the characteristic flow time.

The relaxation times of the chemical reactions (τ_c), vibrational excitation (τ_v), rotational excitation (τ_r), and translation (τ_t) increase in the following order: $\tau_t < \tau_r < \tau_v < \tau_c$ [24, 25]. Thus, as shown in Fig. 2, during the Apollo atmospheric reentry, it gradually experienced thermochemical nonequilibrium flow, chemical nonequilibrium flow, and thermochemical equilibrium flow.

The common application range of the CFD method is $Kn < 0.1$ [26]. Conventional N-S equations are recommended when $Kn < 0.001$ [8], in which sufficient gas particles occupy an element. Under this condition, despite the presence of vibrational excitation and chemical reactions owing to the high temperature, the equilibrium state is quickly achieved. When $0.001 < Kn < 0.1$, the chemical reactions and vibrational excitation require more time to achieve the equilibrium state, during which

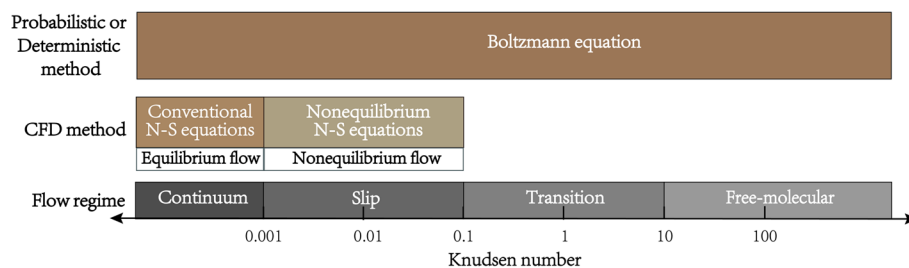


Fig. 3 Validity range of different flow equations

the flow moves downstream [3]; hence the flow field presents a nonequilibrium state. Thus, nonequilibrium N-S equations should be adopted when $0.001 < Kn < 0.1$. When $0.001 < Kn < 0.1$, the shear stress and heat flux predicted by the N-S equations with Newtonian and Fourier models are no longer accurate [27]. Thus, the slip boundary conditions should be considered [28].

As shown in Fig. 3, the Boltzmann equation can be applied to the whole Kn , which can accurately describe the microscopic molecular transport in various flow regimes. It is expressed as [29]

$$\frac{\partial f}{\partial t} + u_i \frac{\partial f}{\partial x_i} = Q(f, f), \quad (3)$$

where $f=f(\mathbf{x}, \mathbf{u}, t)$ is the distribution function at position \mathbf{x} and velocity \mathbf{u} , and $Q(f, f)$ is the collision operator.

There are two types of numerical methods for solving the Boltzmann equation: probabilistic methods such as the DSMC method [26], and deterministic methods such as the discrete velocity method (DVM) [30]. The DSMC method tracks the movements and collisions of individual molecules, and treats molecular collisions using stochastic rather than deterministic procedures to simulate gas flows at the molecular level. The DVM directly solves the Boltzmann equation by the regular numerical discretization of the particle velocity space. However, the conventional DVM performs a slow convergence rate in the near-continuum flow regime owing to the cell size and time step being constrained by the particle mean free path and mean collision time. To improve the efficiency of the DVM in the near-continuum flow regime, Xu [31] proposed the unified gas-kinetic scheme (UGKS). The UGKS couples the particle transport and collision, making the cell size and time step independent of the particle mean free path and collision time. Thus, it has become an efficient DVM-type multiscale method for flow simulation in the entire flow regime.

The predictions of the DSMC method and DVM are consistent with those obtained by the CFD method at a low Kn because the Boltzmann equation can be reduced to the N-S equations through the Chapman–Enskog theory [7]. However, the numerical solution of the Boltzmann equation, either by the DSMC method or DVM, has a high computational cost for large-scale complex geometric models at a low Kn . The N-S equations have a high computational efficiency but cannot accurately describe the characteristics of the rarefied gas in the slip and early transition regimes. The construction of appropriate macroscopic fluid equations to describe the rarefied gas at a lower computational cost has been discussed by many researchers. The moment method is the most effective approach, which reduces the Boltzmann equation to a set of moment equations by expanding the distribution function. Based on the moment method, well-known macroscopic fluid equations have been proposed, such as the Grad13 [32], R13 [33], and R26 [34] moment equations.

Several flow regimes may simultaneously exist in the flow around hypersonic vehicles. Locally rarefied flow may exist in the shock layer, boundary layer, and wake of the body [35]. Because a constant characteristic length was employed, the Kn could

not distinguish the flow regimes in different regions of hypersonic flows over vehicles. Boyd and Wang [36, 37] proposed the gradient-length local Knudsen number Kn_{GLL} to determine the regions where the CFD method can be applied. It is expressed as

$$Kn_{GLL,Q} = \frac{\lambda}{Q} \left| \frac{dQ}{dl} \right|, \quad (4)$$

$$Kn_{GLL} = \max(Kn_{GLL,D}, Kn_{GLL,T}, Kn_{GLL,V}), \quad (5)$$

where Q denotes the flow properties (density D , temperature T , and velocity V), and l is the distance between two points in the flow field.

Boyd [36] investigated the one-dimensional normal shock waves and two-dimensional bow shock waves formed by the flow of argon and nitrogen over a sphere. Wang [37] conducted a numerical study of hypersonic nitrogen flows over an axisymmetric sharp cone tip and a hollow cylinder/flare configuration [37]. Both studies were conducted using the CFD and DSMC methods, and concluded that the continuum approach would break down when the value of Kn_{GLL} exceeded 0.05.

4 Thermochemical equilibrium flow

4.1 Conventional Navier–Stokes equations

As shown in Fig. 2, the thermochemical equilibrium flow mainly exists at a low altitude below 40 km and/or over hypersonic vehicles with a speed below 4 km/s [38], where sufficient collisions occur between particles to establish the equilibrium of various energy modes and make the chemical reactions independent of time. The various internal energies of the gas, including the translational, rotational, vibrational, and electronic energies, can be expressed by a single temperature [39]. The relevant chemical reactions have been fully carried out, which showed that the gas composition is dependent only on the temperature and pressure, which enables the uncoupling of the chemical reactions and flow equations [40]. Consequently, the assumption of thermochemical equilibrium allows the governing equations to be written in a form with a single temperature and without individual species concentrations [41]. In other words, conventional N-S equations can be applied.

The master equations of the thermochemical equilibrium flow are the same as those of the perfect gas, including the mass conservation, moment conservation, and energy conservation equations expressed as Eqs. (6)–(8), respectively.

$$\frac{\partial \rho}{\partial t} + \frac{\partial (\rho u_j)}{\partial x_j} = 0, \quad (6)$$

$$\frac{\partial}{\partial t} (\rho u_i) + \frac{\partial}{\partial x_j} (\rho u_i u_j + p \delta_{ij} - \tau_{ij}) = 0, \quad (7)$$

$$\frac{\partial E}{\partial t} + \frac{\partial}{\partial x_j} ((E + p) u_j - \tau_{ij} u_i + q_j) = 0, \quad (8)$$

where ρ is the density (kg/m^3), u_i and u_j are the velocity vectors (m/s), δ_{ij} is the Kronecker delta, τ_{ij} is the shear stress tensor, p is the pressure (Pa), E is the total energy per unit volume ($\text{kg}/(\text{m}\cdot\text{s}^2)$), and q_j is the heat conduction vector.

Figure 4 shows the computation process of the CFD method for the thermochemical equilibrium flow. Accurate inputs of the gas properties, including the thermodynamic and transport properties, are the key for the predictions of aerodynamic parameters. The thermodynamic and transport properties can be obtained in three ways. The first is to directly obtain these from given tables, in which the properties are dependent only on the temperature and pressure, such as Hasen’s table for 7-species air and Peng–Pindroh’s table for 9-species air. The second method is to calculate these properties using curve-fitting formulas. The third method is to derive them from individual species by the corresponding mixing rules, which requires the chemical composition. Owing to the assumption of chemical equilibrium, the master equations of the chemical composition are independent of the flow equations. The three techniques for calculating the chemical composition are the equilibrium constant method [3], minimization of Gibbs free-energy method [42], and element potential method [43].

4.2 Chemical compositions

For the equilibrium constant method, each occurring chemical reaction must be provided, and the related equilibrium constants are required. In contrast, the minimization of Gibbs free-energy and element potential methods only require knowledge of the elements of reactants and the species of products, which simplifies the calculation process and reduces the calculation time to a certain extent.

Some popular programs can directly provide the chemical composition, such as the CHEMKIN-II [44], NASA CEA [42], and STANJAN [45].

4.2.1 Equilibrium constant method

The chemical composition of a mixture includes NS species and NE elements. NR chemical reactions occur in the mixture. For the chemical reaction i , the related equilibrium constant $K_{p,i}$ can be written as

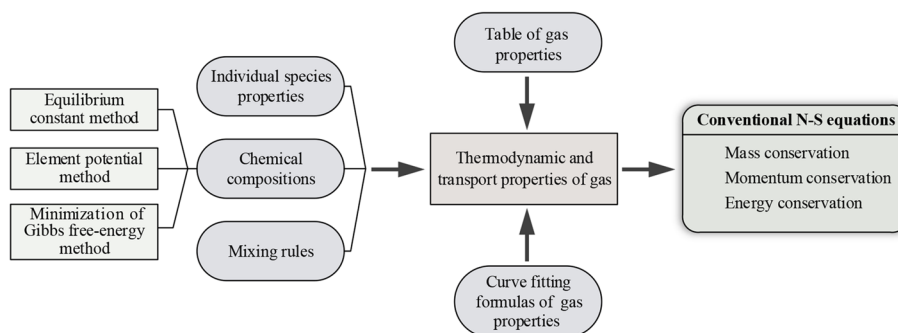


Fig. 4 Diagram of the CFD method for the thermochemical equilibrium flow

$$\prod_i p_j^{\nu_j} = K_{p,i}(T), \quad (9)$$

where ν_j is the stoichiometric mole number of species j which is negative for the reactants and positive for the products, p_j is the partial pressure of species j , and $K_p(T)$ is the equilibrium constant of the given chemical reaction which can be obtained from experiments or calculated by statistical thermodynamics.

According to Dalton's law of partial pressure, the pressure of the mixture can be written as

$$p = \sum_{j=1}^{NS} p_j. \quad (10)$$

However, the number of unknowns is NS , and the number of equations is only $NR + 1$; thus, $NS - NR - 1$ equations are required for a closed form. The number ratios of different elements are known quantities that can be expressed as functions of the partial pressure of the products as

$$\frac{N_m}{N_k} = \frac{\sum_{j=1}^{NS} n_{mj} p_j}{\sum_{j=1}^{NS} n_{kj} p_j}, \quad (11)$$

where N_m and N_k are the numbers of elements m and k , respectively. n_{mj} and n_{kj} are the numbers of elements m and k in species j , respectively.

Finally, the partial pressure of species j , denoted as p_j , can be solved, so the corresponding mass fraction can be easily calculated.

4.2.2 Minimization of Gibbs free-energy method

Gordon and McBride [42, 46] discussed the minimization of Gibbs free energy method in detail and applied it to the NASA Chemical Equilibrium and Application (CEA) computer program. Based on the mass conservation of elements and minimization of the Gibbs free energy theory, the final derived equations are

$$b_i = \sum_{j=1}^{NS} n_{ij} \eta_j, \quad (12)$$

$$\mu_j^0(T) + \mathcal{R}T \ln(\eta_j) + \mathcal{R}T \ln(p) + \sum_{i=1}^{NE} \lambda_i n_{ij} = 0, \quad (13)$$

where b_i is the moles of element i per unit mass, n_{ij} is the stoichiometric coefficient, which represents the number of element i of species j , η_j is the moles of species j per unit mass, $\mu_j^0(T)$ is the temperature-dependent part of the chemical potential per unit mole

(J/mol), \mathcal{R} is the universal gas constant (8314 J/(mol·K)), λ_i is the Lagrangian multiplier (J/mol).

As shown in Eqs. (12) and (13), the $NS + NE$ equations must be solved to obtain η_j and λ_i . Finally, the chemical compositions can be obtained from η_j .

4.2.3 Element potential method

The element potential method is also based on the minimization of the Gibbs free energy, which attempts to do so by arbitrarily changing the quantity of each element. In this method, the element potential ϕ_i is proposed, which requires element conservation equations so that the number of equations to be solved is less than that of minimization of Gibbs free-energy method.

The mole fraction of species j , denoted as X_j , can be expressed as a function of the element potential and Gibbs free energy as [43]

$$X_j = \sum_{j=1}^{NS} \exp\left(\frac{-g_j^\circ}{\mathcal{R}T} + \sum_{i=1}^{NE} \phi_i n_{ij}\right), \quad (14)$$

where g_j° is the molar Gibbs free energy of individual chemical species (J/mol), and ϕ_i is the element potential of element i .

According to the law of mass conservation, the moles of element i in a mixture a_i can be written as

$$a_i = \sum_{j=1}^{NS} n_{ij} \mathcal{N}_{\text{tot}} \exp\left(\frac{-g_j^\circ}{\mathcal{R}T} + \sum_{i=1}^{NE} \phi_i n_{ij}\right), \quad (15)$$

where \mathcal{N}_{tot} is the total moles of the mixture.

The sum of the mole fractions of all species in the mixture is unity; therefore, an additional equation can be written as

$$\sum_{j=1}^{NS} \exp\left(\frac{-g_j^\circ}{\mathcal{R}T} + \sum_{i=1}^{NE} \phi_i n_{ij}\right) = 1. \quad (16)$$

As shown in Eqs. (15) and (16), $NE + 1$ equations can be used to solve ϕ_i , and the corresponding mole fraction of each species can be calculated by Eq. (14).

4.3 Thermodynamic and transport properties of air

As shown in Fig. 4, there are three methods to obtain the transport and thermodynamic properties of the thermochemical equilibrium flow: obtained directly from the given tables, calculated by curve-fitting formulas, and directly calculated based on the statistical thermodynamics theory and collision integrals.

Based on statistical thermodynamics, the thermodynamic properties of individual species can be calculated using related partition functions (see Section 5.3). Based on the kinetic theory, the transport properties of individual species and a mixture can be directly calculated using collision integrals (see Section 5.4). The accuracy of thermodynamic and transport properties is strongly dependent on the appropriate partition functions and precise collision integrals. For a mixture, the accuracy of the gas composition

Table 1 Thermodynamic and/or transport properties of the thermochemical equilibrium flow

Model	Species	Temperature range (K)	Pressure range (atm)	Form
Hansen [47]	N_2, O_2, N, O, N^+, O^+ , and e^-	500 – 15000	$10^{-4} - 10^2$	Table
Peng–Pindroh [48]	$N_2, O_2, N, O, NO, N^+, O^+, NO^+$, and e^-	500 – 15000	$10^{-5} - 10$	Table
Srinivasan [49, 50]	$N_2, O_2, N, O, NO, N^+, O^+, NO^+$, and e^-	500 – 25000	$10^{-7} - 10^3$	Curve-fitted
Gupta [41, 51]	$N_2, O_2, N, O, NO, N^+, O^+, NO^+, O^{2+}, N^{2+}$, and e^-	500 – 30000	$10^{-4} - 10^2$	Curve-fitted
Bacri [52, 53]	$N_2, N_2^+, N, N^+, N^{2+}, N^{3+}, O_2, O_2^+, O_2^-, O, O^-, O^+, O^{2+}, O^{3+}, NO, NO^+, NO^-, NO_2, NO_2^+, NO_2^-, N_2O, N_2O^+, N_2O^-, Ar, Ar^{2+}, Ar^{3+}$, and e^-	1000 – 30000	1 – 200	Graphic
Murphy [54]	$N_2, N_2^+, N, N^-, N^+, N^{2+}, N^{3+}, O_3, O_2, O_2^+, O_2^-, O, O^-, O^+, O^{2+}, O^{3+}, Ar, Ar^+, Ar^{2+}, Ar^{3+}, C, C_2, C_3, C_4, C_5, C^-, C^+, C^{2+}, C_2^-, NO, NO^+, NO_2, NO_2^-, NO_3, NO_3^-, N_2O, N_2O^+, CN, CO, CO^+, CO_2, CO_2^-, C_2O, C_3O_2$, and e^-	300 – 30000	1	Graphic
Capitelli [55]	$N_2, N_2^+, N, N^+, N^{2+}, N^{3+}, N^{4+}, O_2, O_2^+, O_2^-, O, O^-, O^+, O^{2+}, O^{3+}, O^{4+}, NO, NO^+$, and e^-	50 – 100000	1	Table and Curve-fitted
D'Angola [56]	$N_2, N_2^+, N, N^+, N^{2+}, N^{3+}, N^{4+}, O_2, O_2^+, O_2^-, O, O^-, O^+, O^{2+}, O^{3+}, O^{4+}, NO, NO^+$, and e^-	50 – 60000	$10^{-2} - 10^2$	Curve-fitted

is another important factor in calculating the thermodynamic and transport properties. Therefore, researchers have improved the accuracy of thermodynamic and transport property calculations by using more accurate collision integrals and considering more components existed in the gas. For air, the related researches on the thermodynamic and transport properties are summarized in Table 1.

For the convenience of engineering applications, some references present the thermodynamic and/or transport properties of air in a tabulated form, such as Hansen’s table [47] for 7-species air and Peng–Pindroh’s table [48] for 9-species air. However, the table-lookup process is often cumbersome when performing CFD calculations. Based on the tabulated values, simple closed-form equations can be obtained by the curve-fitting approach, which can be incorporated into existing numerical codes. Based on Peng–Pindroh’s [48] tabulated data, Srinivasan [49] developed improved curve-fitting formulas for the transport properties of 9-species air using Grabau-type transition functions. Based on the NASA RGAS data [57], Srinivasan [50] also curve-fitted the thermodynamic properties of 9-species air. Gupta [41, 51] calculated the thermodynamic and transport

properties of 11-species air from 500 to 30,000 K at a pressure range of 10^{-4} to 10^2 atm, and curve-fitted these properties as functions of the temperature at a constant pressure.

When the air temperature exceeds 10,000 K, more ions are produced, which influence the thermodynamic and transport properties. Therefore, more compositions should be taken into account. Bacri [52, 53] calculated the thermodynamic and transport properties of 28-species air at 1 – 200 atm and 1000 – 30,000 K, and presented these properties in graphic forms. Murphy [54] calculated the transport properties of 45-species air at atmospheric pressure and 300 – 30,000 K, in which argon and carbon species were considered. Capitelli [55] calculated the transport properties of 19-species air at 50 – 100,000 K, and reported the corresponding transport properties at 50 – 30,000 K in a table. Capitelli also provided the curve-fitting expressions for these properties based on the calculated data. D'Angola [56] calculated the thermodynamic and transport properties of 19-species air at 0.01 – 100 atm and 50 – 60,000 K, and provided the corresponding curve-fitting expressions.

5 Nonequilibrium flows

As shown in Fig. 2, nonequilibrium flows (thermochemical nonequilibrium flow and chemical nonequilibrium flow) exist at a high attitude owing to the rarefied gas environment. How to accurately describe the nonequilibrium characteristics, such as the nonequilibrium of different energies and inadequate chemical reactions, with numerical models is critical to the prediction of aerodynamic parameters.

To date, various CFD solvers have been developed by some universities and scientific research institutions for nonequilibrium flows in the near-continuum regime. These include some proprietary solvers, such as NASA Langley code LAURA [58], NASA Ames code DPLR [59], Le-MANS [60] developed by the University of Michigan, US3D [61] developed by the University of Minnesota, and the DLR-TAU [62] developed by the German Aerospace Center. Open-source solvers have also been developed, such as the Eilmer [63] developed by the University of Queensland, COOLfluid [64] created by the Von Karman Institute, and Hy2Foam [65, 66] developed by the University of Strathclyde. Meanwhile, software packages have been developed to provide the gas properties of nonequilibrium flows and species production rates, such as the CEA [46] developed by the Lewis Research Center, Cantera [67] sponsored by NumFOCUS, KAPPA [68] created by the Saint Petersburg State University, and Mutation++ [14] developed by the von Karman Institute for Fluid Dynamics.

5.1 Nonequilibrium Navier–stokes equations

In general, there are three types of nonequilibrium equations to describe nonequilibrium flows: one-temperature model [11], two-temperature model [12], and three-temperature model [13]. These three models are based on the assumption of chemical nonequilibrium, which requires the continuity equations of individual species. Based on the molecular dynamics theory, diatomic molecules have various energy modes, including translational, rotational, vibrational, and electronic modes [69], which should be expressed in terms of their respective temperatures. If these energies achieve equilibrium within the flow characteristic time, i.e., the thermal equilibrium state, then the

one-temperature model can be applied; otherwise, the multitemperature models (two- and three-temperature models) should be used. In other words, the one-temperature model should be applied to a chemical nonequilibrium flow, while a multitemperature model should be applied to a thermochemical nonequilibrium flow.

In the one-temperature model, only one temperature T is required to describe all the energies that exist in the gas because of the assumption of thermal equilibrium. In the three-temperature model [13, 70, 71], the first temperature is the translational-rotational temperature T_{tr} , which characterizes the translational energy of the heavy species and the rotational energy of the molecules, in which the translational and rotational temperatures are assumed to be in equilibrium at all times. The second temperature is the vibrational temperature T_v , which characterizes the vibrational energy of molecules. The third temperature is the electron-electronic temperature T_{ele} , which characterizes the free electronic translational energy and electronic excitation energy of the heavy species. The two-temperature model [12, 72] is derived from the three-temperature model by assuming that the vibrational temperature is equal to the electron-electronic temperature. One temperature is the translational-rotational temperature T_{tr} ; the other is the vibrational-electron-electronic temperature T_{ve} that describes the vibrational, electron translational, and electronic excitation energies.

Regardless of the model used to solve the nonequilibrium flows, the conservation of the mass of individual species (Eq. (17)), momentum (Eq. (18)), and total energy (Eq. (19)) must be ensured. The vibrational-electronic energy conservation equation (Eq. (20)) must be added to the two-temperature model, while the vibrational (Eq. (21)) and electron-electronic energy ((Eq. (22)) conservation equations should be added to the three-temperature model. Therefore, the master equations for the three models are as follows:

- (1) One-temperature model \rightarrow Eqs. (17)–(19).
- (2) Two-temperature model \rightarrow Eqs. (17)–(20).
- (3) Three-temperature model \rightarrow Eqs. (17)–(19), (21), and (22).

Figure 5 shows the calculation process of the CFD method for nonequilibrium flows. The master equations are nonequilibrium N-S equations, in which the numerical model (one-, two-, or three-temperature model) can be determined by the corresponding nonequilibrium characteristics. The gas properties, including the thermodynamic and transport properties, can be treated as the input parameters of the master equations and calculated by various techniques. The chemical reaction source can be obtained by different chemical kinetic models. The sources of the vibrational-electronic, vibrational, and electron-electronic energy equations can be obtained by the corresponding energy transfer model. These related numerical models of gas properties and sources presented in Fig. 5 will be reviewed in detail in the following sections.

$$\frac{\partial \rho_s}{\partial t} + \frac{\partial}{\partial x_j} (\rho_s u_j + J_{s,j}) = \dot{w}_s \quad (17)$$

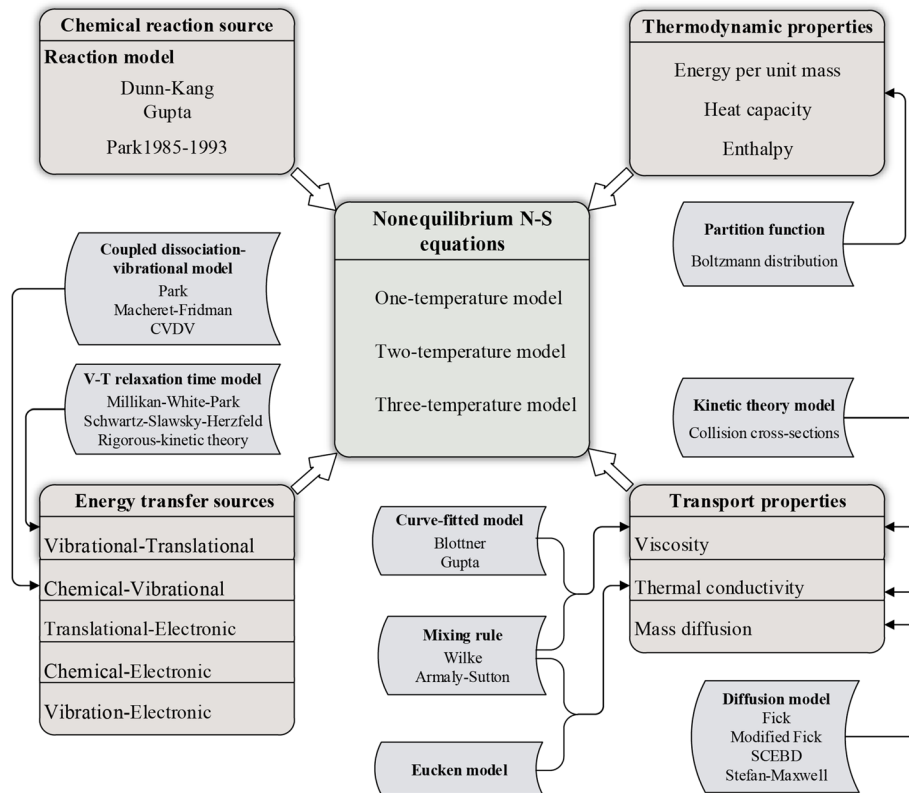


Fig. 5 Diagram of the calculation process of the CFD method for nonequilibrium flows

$$\frac{\partial}{\partial t}(\rho u_i) + \frac{\partial}{\partial x_j}(\rho u_i u_j + p \delta_{ij} - \tau_{ij}) = 0 \quad (18)$$

$$\frac{\partial E}{\partial t} + \frac{\partial}{\partial x_j} \left((E + p) u_j - \tau_{ij} u_i + q_j + \sum_{s=1}^{ns} J_{s,j} h_s \right) = 0 \quad (19)$$

$$\frac{\partial E_{ve}}{\partial t} + \frac{\partial}{\partial x_j} \left(E_{ve} u_j + q_{ve,j} + \sum_{s=1}^{ns} J_{s,j} h_{ve,s} \right) + p_e \frac{\partial u_j}{\partial x_j} = Q_{ve} \quad (20)$$

$$\frac{\partial E_v}{\partial t} + \frac{\partial}{\partial x_j} \left(E_v u_j + q_{v,j} + \sum_{s=1}^{ns} J_{s,j} h_{v,s} \right) = Q_v \quad (21)$$

$$\frac{\partial E_e}{\partial t} + \frac{\partial}{\partial x_j} \left[(E_e + p_e) u_j + q_{e,j} + \sum_s J_{s,j} h_{e,s} \right] - u_j \frac{\partial p_e}{\partial x_j} = Q_e \quad (22)$$

5.2 Chemical reactions

The net source of the chemical species s due to chemical reactions denoted by \dot{w}_s (kg/(m³·s)) can be expressed in terms of the reaction rates as [73]

$$\dot{w}_s = M_s \sum_{r=1}^{NR} (v''_{s,r} - v'_{s,r}) \left[k_{f,r} \prod_{s=1}^{NS} \left(\frac{\rho_s}{M_s} \right)^{v'_{s,r}} - k_{b,r} \prod_{s=1}^{NS} \left(\frac{\rho_s}{M_s} \right)^{v''_{s,r}} \right], \quad (23)$$

where $v''_{s,r}$ and $v'_{s,r}$ are the forward and backward stoichiometric coefficients of species s in the reaction r , k_f and k_b represent the forward and backward reaction rate coefficients ($\text{m}^3 \cdot \text{s}^{-1} \cdot \text{mol}^{-1}$), respectively, M_s is the molecular weight of species s (kg/mol).

Since the 1970s, various chemical kinetic models have been proposed to evaluate the k_f and k_b of air. Blottner [74] developed a chemical kinetic model for 7-species air (N_2 , O_2 , NO , N , O , NO^+ , and e^-), with seven elementary reactions. Dunn and Kang [75] proposed a chemical model for 11-species air (N_2 , O_2 , NO , N , O , NO^+ , N_2^+ , O_2^+ , N^+ , O^+ , and e^-), which includes 26 elementary reactions. In the Dunn–Kang model, both the k_f and k_b were evaluated by the Arrhenius law. Based on the Blottner and Dunn–Kang models, Gupta [51] proposed a chemical kinetic model for 11-species air containing 20 elementary reactions. The forward reaction rate coefficients of the first seven reactions were obtained from the Blottner model, while those of the remaining reactions were obtained from the Dunn–Kang model. Gupta considered that the backward reaction rate was dependent on the forward reaction rate, and proposed an equilibrium constant method to calculate the backward reaction rate coefficients. Park proposed the Park1985 [76], Park1987 [77], Park1989 [78], Park1991 [79], and Park1993 [16] models for 11-species air, and the Park2001 [80] model that considers the ablating heat shield. Similar to the Gupta model, the backward reaction rate coefficients in the models were calculated by the equilibrium constant method.

All of the above chemical kinetic models have clear parameter tables in formula form, which can be directly used to calculate the reaction rate coefficients. However, some reactions were excluded from these models, especially ionization reactions. Owing to the uncertainty of the measurements, it is impractical to obtain the reaction rate coefficients experimentally. A feasible method is to obtain the reaction rates at several temperatures by the DSMC method, and then curve-fitting these results as a function of the temperature, such as Ozawa's modified model [81] and the Q-K model [82].

The forward rate coefficient k_f in the above models is assumed to follow the Arrhenius law expressed as

$$k_f = A_f \times T_{c,f}^{B_f} \exp\left(-\frac{T_a}{T_{c,f}}\right), \quad (24)$$

where A_f is a pre-exponential factor, B_f is the temperature exponent, T_a is the temperature of activation derived from the activation energy, and $T_{c,f}$ is the controlling temperature of the forward reaction.

The backward rate coefficient k_b can be calculated by two methods. One method assumes that the k_b follows the Arrhenius law and is independent of the k_f , such as the Dunn–Kang model. It is written as [75]

$$k_b = A_b \times T_{c,b}^{B_b} \exp\left(-\frac{T_b}{T_{c,b}}\right). \quad (25)$$

However, this form is inappropriate for high velocities [51]. The other method assumes that the k_b is a function of the k_f such as Gupta model and Park models, and is written as [51, 76]

$$k_b = \frac{k_f}{K_{eq}}, \quad (26)$$

where K_{eq} is the equilibrium constant calculated as a function of the temperature. Two expressions proposed by Gupta (Eq. (27)) and Park (Eq. (28)) are commonly used in relevant research, and are written as [51, 76]

$$K_{eq} = \exp(A_1 Z^5 + A_2 Z^4 + A_3 Z^3 + A_4 Z^2 + A_5 Z + A_6), \quad (27)$$

$$K_{eq} = \exp\left(A_1/Z + A_2 + A_3 \ln Z + A_4 Z + A_5 Z^2\right), \quad (28)$$

where $Z = 10^4/T$, and the equilibrium constant coefficient A can be obtained from [51] and [76].

Table 2 summarizes the parameters of the forward rate coefficients evaluated by the Dunn–Kang (1973) [75], Gupta (1990) [51], Park1985 [76], Park1987 [77], Park1989 [78], Park1991 [79], and Park1993 [16] models. As seen in Table 2, the chemical reactions in air can be classified as Dissociation (No. 1–32), NO Exchange (No. 33–34), Associative ionization (No. 35–37), Exchange ionization (No. 38), NO Ionization (No. 39–40), Charge exchange (No. 41–54), and Electron-impact ionization (No. 55–56). Compared with the Dunn–Kang and Gupta models, Park's models considered ions as a third body for dissociation reactions. Although many models have been proposed by Park, the Park1989 and Park1991 models are basically the same as the Park1993 model except for a few reactions.

Figure 6 shows the comparison of the forward rate coefficients of the 5-species air (N_2 , O_2 , NO, N, and O) of the Dunn–Kang, Gupta, and Park1993 models. No obvious difference is observed between the forward rate coefficients of the three models for the chemical reactions in the 5-species air. The O_2 dissociation most likely occurs in the air. The forward rate coefficient obtained by the Gupta model is smaller than those calculated by the Dunn–Kang and Park1993 models.

The influence of the chemical kinetic model on aerodynamic properties has been widely investigated. Wang et al. [83] assessed the performance of four chemical reaction models (Dunn–Kang, Gupta, Park1987, and Park1991 models) of the heat transfer acting on three typical hypersonic vehicles (ELECTRE vehicle, Apollo command module, and Space Shuttle Orbiter), as shown in Fig. 7. Their results showed that the predictions of the heat flux with a complex geometry were more sensitive to the choice of chemical kinetic models. Hao et al. [84] predicted the electron and ion distributions on the RAM-C II vehicle and FIRE II capsule using the Park1989 and Gupta models. Their results showed that the different chemical reaction models significantly affected the ion and electron distributions, as shown in Fig. 8. Niu et al. [85] investigated the influence

Table 2 Forward reaction rate coefficients for air (cm³mole⁻¹sec⁻¹)

No	Reaction	Dunn-Kang [75]			Gupta [51]			Park1985 [76]			Park1987 [77]			Park1989 [78]			Park1991 [79]			Park1993 [16]					
		A _f	B _f	T _a	A _f	B _f	T _a	A _f	B _f	T _a	A _f	B _f	T _a	A _f	B _f	T _a	A _f	B _f	T _a	A _f	B _f	T _a			
1	O ₂ + N ⇌ O + O + N	3.60e18	-1.00	59500	3.61e18	-1.00	59400	8.25e19	-1.0	59500	2.90e23	-2.0	59750	1.00e22	-1.50	59500	1.00e22	-1.50	59500	1.00e22	-1.50	59500	1.00e22	-1.50	59500
2	O ₂ + O ⇌ O + O + O	9.00e19	-1.00	59500	3.61e18	-1.00	59400	8.25e19	-1.0	59500	2.90e23	-2.0	59750	1.00e22	-1.50	59500	1.00e22	-1.50	59500	1.00e22	-1.50	59500	1.00e22	-1.50	59500
3	O ₂ + O ₂ ⇌ O + O + O ₂	3.24e19	-1.00	59500	3.61e18	-1.00	59400	2.75e19	-1.0	59500	9.68e22	-2.0	59750	2.00e21	-1.50	59500	2.00e21	-1.50	59500	2.00e21	-1.50	59500	2.00e21	-1.50	59500
4	O ₂ + N ₂ ⇌ O + O + N ₂	7.20e18	-1.00	59500	3.61e18	-1.00	59400	2.75e19	-1.0	59500	9.68e22	-2.0	59750	2.00e21	-1.50	59500	2.00e21	-1.50	59500	2.00e21	-1.50	59500	2.00e21	-1.50	59500
5	O ₂ + NO ⇌ O + O + NO	3.60e18	-1.00	59500	3.61e18	-1.00	59400	2.75e19	-1.0	59500	9.68e22	-2.0	59750	2.00e21	-1.50	59500	2.00e21	-1.50	59500	1.00e22	-1.50	59500	1.00e22	-1.50	59500
6	O ₂ + N ⁺ ⇌ O + O + N ⁺							8.25e19	-1.0	59500									1.00e22	-1.50	59500	1.00e22	-1.50	59500	
7	O ₂ + O ⁺ ⇌ O + O + O ⁺							8.25e19	-1.0	59500									1.00e22	-1.50	59500	1.00e22	-1.50	59500	
8	O ₂ + N ₂ ⁺ ⇌ O + O + N ₂ ⁺							2.75e19	-1.0	59500									2.00e21	-1.50	59500	2.00e21	-1.50	59500	
9	O ₂ + O ₂ ⁺ ⇌ O + O + O ₂ ⁺							2.75e19	-1.0	59500									2.00e21	-1.50	59500	2.00e21	-1.50	59500	
10	O ₂ + NO ⁺ ⇌ O + O + NO ⁺							2.75e19	-1.0	59500									2.00e21	-1.50	59500	2.00e21	-1.50	59500	
11	O ₂ + e ⁻ ⇌ O + O + e ⁻							1.32e22	-1.0	59500	2.90e23	-2.0	59750												
12	N ₂ + N ⇌ N + N + N	4.09e22	-1.50	113000	4.15e22	-1.50	113100	1.10e22	-1.6	113200	1.60e22	-1.6	113200	3.00e22	-1.60	113200	3.00e22	-1.60	113200	3.00e22	-1.60	113200	3.00e22	-1.60	113200
13	N ₂ + O ⇌ N + N + O	1.90e17	-0.50	113000	1.92e17	-0.50	113100	1.10e22	-1.6	113200	4.98e22	-1.6	113200	3.00e22	-1.60	113200	3.00e22	-1.60	113200	3.00e22	-1.60	113200	3.00e22	-1.60	113200
14	N ₂ + O ₂ ⇌ N + N + O ₂	1.90e17	-0.50	113000	1.92e17	-0.50	113100	3.70e21	-1.6	113200	3.70e21	-1.6	113200	7.00e21	-1.60	113200	7.00e21	-1.60	113200	7.00e21	-1.60	113200	7.00e21	-1.60	113200
15	N ₂ + N ₂ ⇌ N + N + N ₂	4.70e17	-0.50	113000	1.92e17	-0.50	113100	3.70e21	-1.6	113200	3.70e21	-1.6	113200	7.00e21	-1.60	113200	7.00e21	-1.60	113200	7.00e21	-1.60	113200	7.00e21	-1.60	113200
16	N ₂ + NO ⇌ N + N + NO	1.90e17	-0.50	113000	1.92e17	-0.50	113100	3.70e21	-1.6	113200	4.98e21	-1.6	113200	7.00e21	-1.60	113200	7.00e21	-1.60	113200	7.00e21	-1.60	113200	7.00e21	-1.60	113200
17	N ₂ + N ⁺ ⇌ N + N + N ⁺							1.10e22	-1.6	113200									3.00e22	-1.60	113200	3.00e22	-1.60	113200	
18	N ₂ + O ⁺ ⇌ N + N + O ⁺							1.10e22	-1.6	113200									3.00e22	-1.60	113200	3.00e22	-1.60	113200	
19	N ₂ + N ₂ ⁺ ⇌ N + N + N ₂ ⁺							3.70e21	-1.6	113200									7.00e21	-1.60	113200	7.00e21	-1.60	113200	
20	N ₂ + O ₂ ⁺ ⇌ N + N + O ₂ ⁺							3.70e21	-1.6	113200									7.00e21	-1.60	113200	7.00e21	-1.60	113200	
21	N ₂ + NO ⁺ ⇌ N + N + NO ⁺							3.70e21	-1.6	113200									7.00e21	-1.60	113200	7.00e21	-1.60	113200	
21	N ₂ + e ⁻ ⇌ N + N + e ⁻							1.11e24	-1.6	113200	8.30e24	-1.6	113200	9.00e24	-1.6	113200	3.00e24	-1.60	113200	1.20e25	-1.60	113200	1.20e25	-1.60	113200
22	NO + N ⇌ N + O + N	7.80e20	-1.50	75500	3.97e20	-1.50	75600	4.60e17	-0.5	75500	7.95e23	-2.0	75500	1.10e17	0.0	75500	1.10e17	0.0	75500	1.10e17	0.0	75500	1.10e17	0.0	75500
23	NO + O ⇌ N + O + O	7.80e20	-1.50	75500	3.97e20	-1.50	75600	4.60e17	-0.5	75500	7.95e23	-2.0	75500	1.10e17	0.0	75500	1.10e17	0.0	75500	1.10e17	0.0	75500	1.10e17	0.0	75500
24	NO + N ₂ ⇌ N + O + N ₂	3.90e20	-1.50	75500	3.97e20	-1.50	75600	2.30e17	-0.5	75500	7.95e23	-2.0	75500	5.00e15	0.0	75500	5.00e15	0.0	75500	5.00e15	0.0	75500	5.00e15	0.0	75500

Table 2 (continued)

No	Reaction	Dunn-Kang [75]			Gupta [51]			Park1985 [76]			Park1987 [77]			Park1989 [78]			Park1991 [79]			Park1993 [16]		
		A_f	B_f	T_a	A_f	B_f	T_a	A_f	B_f	T_a	A_f	B_f	T_a	A_f	B_f	T_a	A_f	B_f	T_a	A_f	B_f	T_a
25	$\text{NO} + \text{O}_2 \rightleftharpoons \text{N} + \text{O} + \text{O}_2$	3.90e20	-1.50	75500	3.97e20	-1.50	75600	2.30e17	-0.5	75500	7.95e23	-2.0	75500	5.00e15	0.0	75500	5.00e15	0.0	75500	5.00e15	0.0	75500
26	$\text{NO} + \text{NO} \rightleftharpoons \text{N} + \text{O} + \text{NO}$	7.80e20	-1.50	75500	3.97e20	-1.50	75600	2.3e17	-0.5	75500	7.95e23	-2.0	75500	1.10e17	0.0	75500	1.10e17	0.0	75500	1.10e17	0.0	75500
27	$\text{NO} + \text{N}^+ \rightleftharpoons \text{N} + \text{O} + \text{N}^+$							4.60e17	-0.5	75500												
28	$\text{NO} + \text{O}^+ \rightleftharpoons \text{N} + \text{O} + \text{O}^+$							4.60e17	-0.5	75500												
29	$\text{NO} + \text{N}_2^+ \rightleftharpoons \text{N} + \text{O} + \text{N}_2^+$							2.30e17	-0.5	75500												
30	$\text{NO} + \text{O}_2^+ \rightleftharpoons \text{N} + \text{O} + \text{O}_2^+$							2.30e17	-0.5	75500												
31	$\text{NO} + \text{NO}^+ \rightleftharpoons \text{N} + \text{O} + \text{NO}^+$							2.30e17	-0.5	75500												
32	$\text{NO} + \text{e}^- \rightleftharpoons \text{N} + \text{O} + \text{e}^-$							7.36e19	-0.5	75500	7.95e23	-2.0	75500									
33	$\text{NO} + \text{O} \rightleftharpoons \text{N} + \text{O}_2$	3.20e9	1.00	19700	3.18e9	1.00	19700	2.16e8	1.29	19220	8.37e12	0	19450	8.40e12	0.0	19450	8.40e12	0.0	19450	8.40e12	0.0	19450
34	$\text{N}_2 + \text{O} \rightleftharpoons \text{NO} + \text{N}$	7.00e13	0.00	38000	6.75e13	0.00	37500	3.18e13	0.1	37700	6.44e17	-1.0	38370	6.40e17	-1.0	38370	6.40e17	-1.0	38400	6.40e17	-1.0	38400
35	$\text{N} + \text{O} \rightleftharpoons \text{NO}^+ + \text{e}^-$	(1.4±0.4)e6	1.50	31900	9.03e9	0.50	32400	1.53e11	-0.37	32000	1.53e9	0.37	32000	5.30e12	0.0	32000	8.80e8	1.00	31900	8.80e8	1.0	31900
36	$\text{N} + \text{N} \rightleftharpoons \text{N}_2^+ + \text{e}^-$	(1.4±0.3)e13	0.00	67800	(1.4±0.3)e13	0.00	67800	1.79e11	0.77	67500	1.79e9	0.77	67500	2.00e13	0.0	67500	4.40e7	1.50	67500	4.40e7	1.50	67500
37	$\text{O} + \text{O} \rightleftharpoons \text{O}_2^+ + \text{e}^-$	(1.6±0.4)e17	-0.98	80800	(1.6±0.4)e17	-0.98	80800	3.85e11	0.49	80600	3.85e9	0.49	80600	1.10e13	0.0	80600	7.10e2	2.70	80600	7.10e2	2.70	80600
38	$\text{O}_2 + \text{N}_2 \rightleftharpoons \text{NO} + \text{NO}^+ + \text{e}^-$	1.38e20	-1.84	141000	1.38e20	-1.84	141000															
39	$\text{NO} + \text{N}_2 \rightleftharpoons \text{NO}^+ + \text{e}^- + \text{N}_2$	2.20e15	-0.35	108000	2.20e15	-0.35	108000															
40	$\text{NO} + \text{O}_2 \rightleftharpoons \text{NO}^+ + \text{e}^- + \text{O}_2$	8.80e15	-0.35	108000	2.20e15	-0.35	108000															
41	$\text{O} + \text{NO}^+ \rightleftharpoons \text{O}_2 + \text{N}^+$	1.34e13	0.31	77270	1.34e13	0.31	77270															
42	$\text{N}_2 + \text{N}^+ \rightleftharpoons \text{N} + \text{N}_2^+$	2.02e11	0.81	13000	2.02e11	0.81	13000	9.85e12	-0.18	12100	9.85e12	-0.18	12100	1.00e12	0.50	77200	1.00e12	0.50	77200	1.00e12	0.50	77200
43	$\text{N} + \text{O}_2^+ \rightleftharpoons \text{O}_2 + \text{N}^+$																					
44	$\text{NO} + \text{O}^+ \rightleftharpoons \text{O}_2 + \text{N}^+$																					
45	$\text{N}_2 + \text{O}_2^+ \rightleftharpoons \text{O}_2 + \text{N}_2^+$																					
46	$\text{O} + \text{O}_2^+ \rightleftharpoons \text{O}_2 + \text{O}^+$	2.92e18	-1.11	28000	2.92e18	-1.11	28000	6.85e13	-0.52	18600	6.85e13	-0.52	18600	4.00e12	-0.09	18600	4.00e12	-0.09	18000	4.00e12	-0.09	18000

Table 2 (continued)

No	Reaction	Dunn-Kang [75]			Gupta [51]			Park1985 [76]			Park1987 [77]			Park1989 [78]			Park1991 [79]			Park1993 [16]		
		A_f	B_f	T_a	A_f	B_f	T_a	A_f	B_f	T_a	A_f	B_f	T_a	A_f	B_f	T_a	A_f	B_f	T_a	A_f	B_f	T_a
47	$N + NO^+ \rightleftharpoons N_2 + O^+$																					
48	$N + NO^+ \rightleftharpoons NO + N^+$	1.00e19	-0.93	61000	1.00e19	-0.93	61000	2.21e15	-0.02	61100												
49	$N + NO^+ \rightleftharpoons O + N_2^+$							1.7e13	0.4	35500	1.7e13	0.4	35500	1.70e13	0.4	35500	7.20e13	0.00	35500	7.20e13	0.00	35500
50	$O_2 + NO^+ \rightleftharpoons NO + O_2^+$	1.80e15	0.17	33000	1.80e15	0.17	33000	1.03e16	-0.17	32400	1.03e16	-0.17	32400	2.40e13	0.41	32400	2.40e13	0.41	32600	2.40e13	0.41	32600
51	$O + NO^+ \rightleftharpoons NO + O^+$	3.63e15	-0.60	50800	3.63e15	-0.60	50800	2.75e13	0.01	51000	2.75e13	0.01	51000									
52	$O + NO^+ \rightleftharpoons N + O_2^+$																					
53	$N + NO^+ \rightleftharpoons O + N_2^+$																					
54	$N_2 + O^+ \rightleftharpoons O + N_2^+$	3.40e19	-2.00	23000	3.40e19	-2.00	23000	6.33e13	-0.21	22200	6.33e13	-0.21	22200	9.10e11	0.36	22200	9.10e11	0.36	22800	9.10e11	0.36	22800
55	$O + e^- \rightleftharpoons O^+ + e^- + e^-$	(3.6 ± 1.2)e31	-2.91	158000	(3.6 ± 1.2)e31	-2.91	158000	3.9e33	-3.78	158500	3.9e33	-3.78	158500	3.90e33	-3.78	158500	3.90e33	-3.78	158500	3.90e33	-3.78	158500
56	$N + e^- \rightleftharpoons N^+ + e^- + e^-$	(1.1 ± 0.4)e32	-3.14	169000	(1.1 ± 0.4)e32	-3.14	169000	2.5e34	-3.82	168600	2.5e34	-3.82	168600	2.50e33	-3.82	168600	2.50e34	-3.82	168600	2.50e34	-3.82	168600

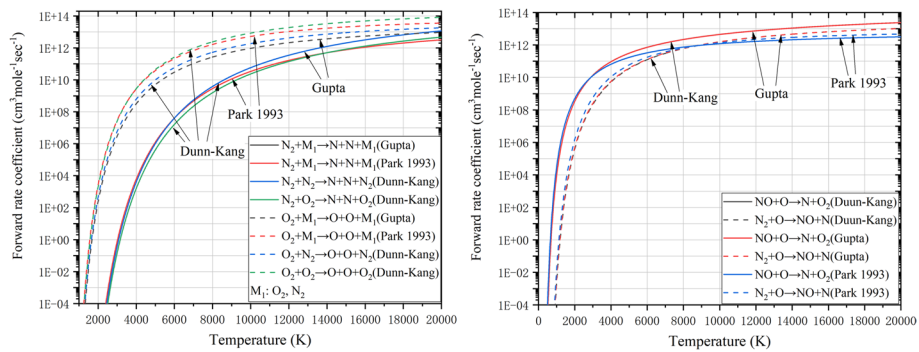


Fig. 6 Forward rate coefficients of the 5-species air of the Dunn–Kang, Park1993, and Gupta models

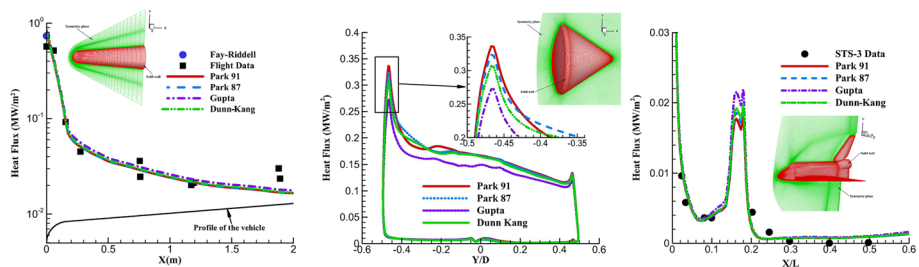


Fig. 7 Heat flux distributions of ELECTRE, Apollo, and Space Shuttle Orbiter with different chemical reaction models [83]

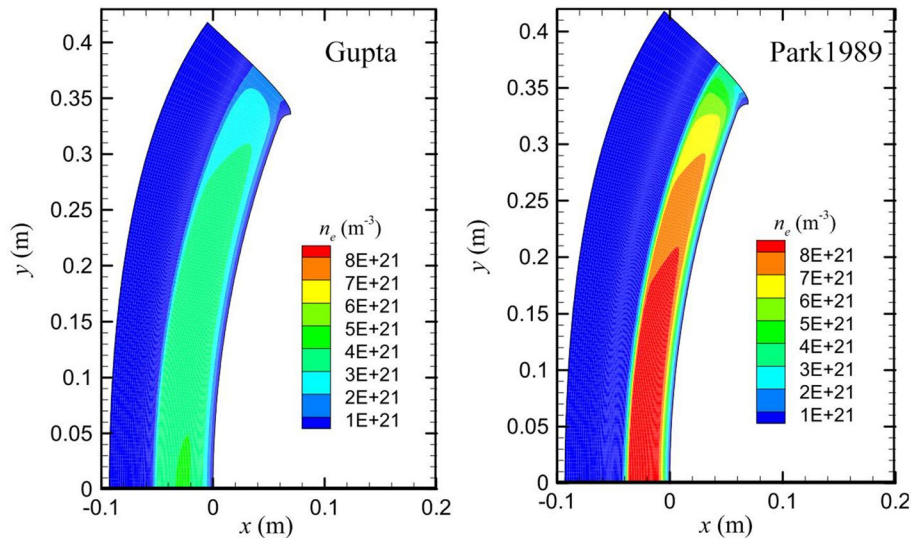


Fig. 8 Electron number density for FIRE II [84]

of three models (Gupta, Park1993, and Ozawa’s modified models) and two controlling temperatures ($T_{tr}^{0.5}T_{ve}^{0.5}$ and $T_{tr}^{0.7}T_{ve}^{0.3}$) on the species concentration and distribution in the shock layer over the BSUV II and RAM-C II vehicles. Their results showed that the NO concentration increased, and the electron density decreased as the T_{tr} weight factor increased. The Ozawa model with the $T_{tr}^{0.7}T_{ve}^{0.3}$ controlling temperature was more effective in predicting the electron formation compared with the other models, as shown in Fig. 9.

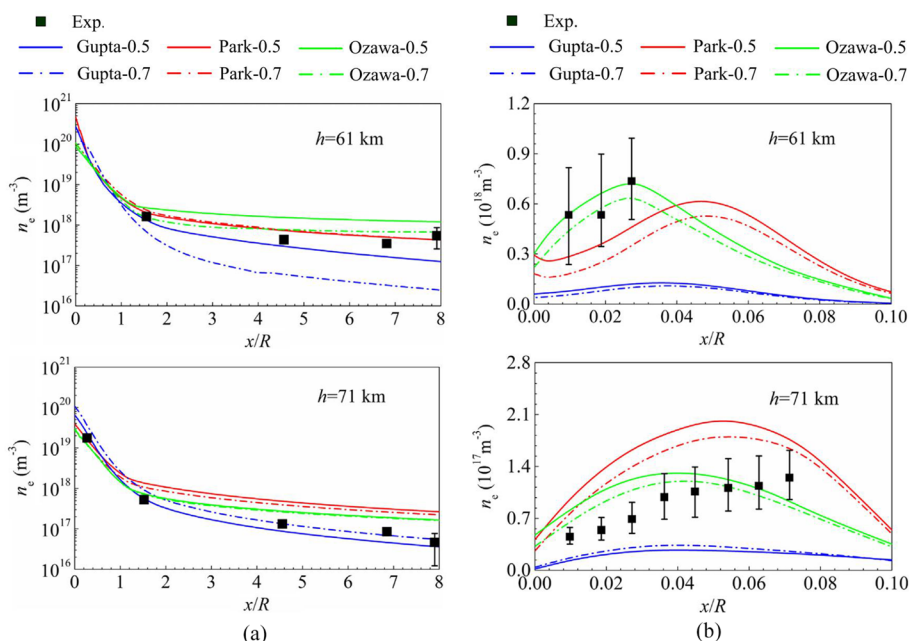


Fig. 9 Electron number density of BSUV-II [85]. (a) Peak electron number density along the surface and (b) electron number density at the location of the electrostatic probe rake

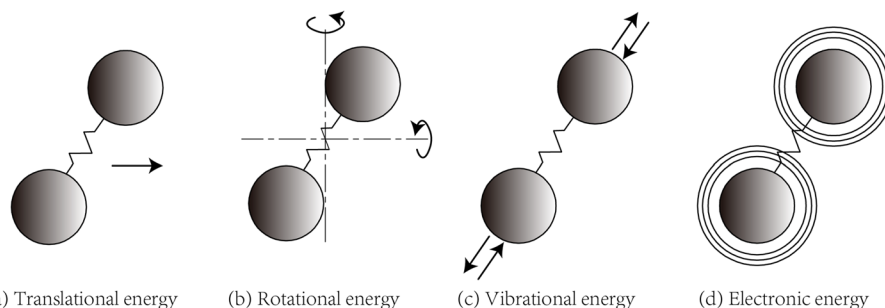


Fig. 10 Energy modes for a diatomic molecule [40]

5.3 Thermodynamic properties

The internal energy of molecules can be regarded as the expression of energy storage and release in various internal modes of molecular motion. Namely, the translation, rotation, vibration of the molecular, as well as the kinetic and potential energies of the electrons around the nucleus [40]. Figure 10 shows these energy modes of a diatomic molecule. In a thermal nonequilibrium flow, the different energy modes should be expressed in terms of their associated temperatures to distinguish their relevant contributions to the basic thermodynamic properties [86]. The thermodynamic properties of individual species, such as the enthalpy, entropy, and specific heats, can be calculated using the formulas from statistical thermodynamics [87], in which the partition-function approach is employed.

According to quantum physics, the energy of a single atom or molecule is a discrete value, which can be calculated by its energy state i . For a system consisting of N

particles, the sensible energy is the sum of the energy of the particles in each energy state. This is expressed as

$$E = \sum_{i=0}^{\infty} \varepsilon_i N_i, \quad (29)$$

where N_i is the number of particles in energy state i , and ε_i is the energy of level i of a particle.

If the distribution of N_i is known, then the sensible internal energy of the system can be calculated. Although many possible distributions of N_i may exist in the system, the most probable macroscopic state exists among all the possible ones, i.e., the equilibrium macroscopic state. This state is given by the Boltzmann distribution as [40]

$$N_i^* = \frac{Ng_i \exp(-\varepsilon_i/kT)}{Q} \quad (30)$$

with

$$Q = \sum_{i=0}^{\infty} g_i \exp(-\varepsilon_i/kT), \quad (31)$$

where Q is the partition function, and g_i is the degeneracy representing the statistical weight in energy state i of the molecule.

The energy per unit mass of an individual species can be directly derived from the internal partition function given by

$$e = RT^2 \left(\frac{\partial \ln Q}{\partial T} \right). \quad (32)$$

According to the related partition function, the rotational ($e_{r,s}$), vibrational ($e_{v,s}$), and electronic ($e_{el,s}$) energies per unit mass of the heavy species s are expressed as [19]

$$e_{r,s} = R_s T_{r,s}, \quad (33)$$

$$e_{v,s} = R_s \frac{\theta_{v,s}}{\exp(\theta_{v,s}/T_{v,s}) - 1}, \quad (34)$$

$$e_{el,s} = R_s \frac{\theta_{el,1,s} (g_{1,s}/g_{0,s}) \exp(-\theta_{el,1,s}/T_{el,s})}{1 + (g_{1,s}/g_{0,s}) \exp(-\theta_{el,1,s}/T_{el,s})}, \quad (35)$$

where $\theta_v = hv/k$ and $\theta_{el} = \varepsilon_i^{el}/k$ are the characteristic vibrational and electronic temperatures, respectively; and R_s is the specific gas constant of species s (J/(kg·K)). Obviously, the values of $e_{r,s}$ and $e_{v,s}$ are zero for atoms and atom ions. Equation (33) was derived from a rigid rotor, and is only valid for homonuclear and heteronuclear molecules with a smaller degeneracy. In Eq. (35), only the first two terms of the partition function were considered, and the electronic energy of the ground state was set to zero.

The expression of $e_{v,s}$ in Eq. (34) was derived from the harmonic oscillator model, where the value $\Delta\varepsilon = \varepsilon_i - \varepsilon_{i-1}$ remains constant for all i . However, the value of $\Delta\varepsilon$ varied

at high temperatures (highly excited states). The anharmonic oscillator model provides a more precise approximation of the real molecular spectra because it considers their refinement for high vibrational levels. In the anharmonic oscillator model, the vibrational energy of a diatomic molecule at level i is written as [24]

$$\frac{\varepsilon_i^V}{hc} = \omega_e \left(i + \frac{1}{2}\right) - \omega_e x_e \left(i + \frac{1}{2}\right)^2 + \omega_e y_e \left(i + \frac{1}{2}\right)^3 + \dots, \quad (36)$$

where ω_e , $\omega_e x_e$, and $\omega_e y_e$ are the spectroscopic constants. If only the first term on the right side of Eq. (36) is considered, it becomes the harmonic oscillator model.

Based on the kinetic theory, $e_{t,s}$ is the translational energy per unit mass of species s written as

$$e_{t,s} = \frac{1}{2} (c_1'^2 + c_2'^2 + c_3'^2) = \frac{3}{2} R_s T_{t,s}. \quad (37)$$

According to Eqs. (33)–(35) and (37), the heat capacities at a constant volume (J/(kg·K)) of the heavy species s in the translational ($Cv_{t,s}$), rotational ($Cv_{r,s}$), vibrational ($Cv_{v,s}$), and electronic ($Cv_{el,s}$) energy modes can be derived as follows:

$$Cv_{t,s} = \frac{3}{2} R_s, \quad (38)$$

$$Cv_{r,s} = R_s, \quad (39)$$

$$Cv_{v,s} = R_s \frac{\theta_{v,s}/2T_{v,s}}{\sinh(\theta_{v,s}/2T_{v,s})}, \quad (40)$$

$$Cv_{el,s} = R_s \frac{(-\theta_{el,1,s}/T_{el,s})^2 (g_{1,s}/g_{0,s}) \exp(-\theta_{el,1,s}/T_{el,s})}{[1 + (g_{1,s}/g_{0,s}) \exp(-\theta_{el,1,s}/T_{el,s})]^2}. \quad (41)$$

According to Eqs. (38)–(41), the total contribution of the translational and rotational motions to the specific heat is $2.5R$ for molecules and $1.5R$ for atoms, respectively.

The heat capacities at constant pressure (J/(kg·K)) of species s in different energy modes are defined as

$$Cp_{t,s} = Cv_{t,s} + R_s, \quad (42)$$

$$Cp_{r,s} = Cv_{r,s}, Cp_{v,s} = Cv_{v,s}, Cp_{el,s} = Cv_{el,s}. \quad (43)$$

The enthalpy at various energy modes for species s can be written as

$$h_{t,s} = Cp_{t,s} T_t, \quad (44)$$

$$h_{r,s} = e_{r,s}, h_{v,s} = e_{v,s}, h_{el,s} = e_{el,s}. \quad (45)$$

The electron heat capacities at constant volume and pressure are expressed as [71]

$$Cv_e = \frac{3}{2} R_e, \quad (46)$$

$$Cp_e = \frac{5}{2} Re. \quad (47)$$

5.4 Transport properties

The transport properties (e.g., viscosity, thermal conductivity, and diffusion coefficient) determine the reliability of the viscous stress, heat conduction, and species diffusion results, particularly in the boundary layers and shock waves. These transport properties can be directly calculated by collision integrals or certain empirical formulas. The following subsections will review the corresponding calculation methods for the transport properties of individual and multicomponent species.

5.4.1 Viscous stress and heat conduction

As shown in the nonequilibrium N-S equations, τ_{ij} represents the components of the viscous stress tensor written as

$$\tau_{ij} = \mu \left(\frac{\partial u_i}{\partial x_j} + \frac{\partial u_j}{\partial x_i} \right) - \frac{2}{3} \mu \frac{\partial u_k}{\partial x_k} \delta_{ij}, \quad (48)$$

where μ is the viscosity (kg/(m·s)).

The total heat conduction vector q_j is the sum of the heat conduction in different energy modes, each of which is assumed to follow Fourier's law:

$$q_j = -\kappa_t \frac{\partial T_t}{\partial x_j} - \kappa_r \frac{\partial T_r}{\partial x_j} - \kappa_v \frac{\partial T_v}{\partial x_j} - \kappa_{el} \frac{\partial T_{el}}{\partial x_j} - \kappa_e \frac{\partial T_e}{\partial x_j}, \quad (49)$$

where κ_t , κ_r , κ_v , κ_{el} , and κ_e are the translational, rotational, vibrational, electronic, and electron thermal conductivities (J/(m·s·K)), respectively.

For the one-temperature model, Eq. (49) can be written as

$$q_j = -(\kappa_t + \kappa_r + \kappa_v + \kappa_{el} + \kappa_e) \frac{\partial T}{\partial x_j} = -\kappa \frac{\partial T}{\partial x_j}. \quad (50)$$

For the two-temperature model, Eq. (49) can be written as

$$q_j = q_{tr,j} + q_{ve,j} = -(\kappa_t + \kappa_r) \frac{\partial T_{tr}}{\partial x_j} - (\kappa_v + \kappa_{el} + \kappa_e) \frac{\partial T_{ve}}{\partial x_j} = -\kappa_{tr} \frac{\partial T_{tr}}{\partial x_j} - \kappa_{ve} \frac{\partial T_{ve}}{\partial x_j}. \quad (51)$$

For the three-temperature model, Eq. (49) can be written as

$$q_j = q_{tr,j} + q_{v,j} + q_{e,j} = -(\kappa_t + \kappa_r) \frac{\partial T_{tr}}{\partial x_j} - \kappa_v \frac{\partial T_v}{\partial x_j} - (\kappa_{el} + \kappa_e) \frac{\partial T_e}{\partial x_j} = -\kappa_{tr} \frac{\partial T_{tr}}{\partial x_j} - \kappa_v \frac{\partial T_v}{\partial x_j} - \kappa_{ele} \frac{\partial T_{ele}}{\partial x_j}, \quad (52)$$

where κ , κ_{tr} , κ_{ve} , κ_v , and κ_{ele} are the total, translational-rotational, vibrational-electron-electronic, vibrational, and electron-electronic thermal conductivities, respectively.

Because air is a mixture of gases, the viscosity and thermal conductivities applied in air are mixed quantities. The viscosity and thermal conductivities of a mixture can be

obtained by two methods: one is derived from individual species quantities using mixing rules, and the other is directly calculated by collision integrals.

5.4.2 Viscosity of individual species

Based on the kinetic theory, the viscosity of the heavy species s can be calculated by solving the Boltzmann equation using the Chapman–Enskog method, which is expressed as [38]

$$\mu_s = \frac{5}{16} \frac{\sqrt{\pi m_s k T}}{\overline{Q_{s,s}}^{(2,2)}}, \tag{53}$$

where m_s is the mass of species s (kg/particle), k is the Boltzmann’s constant, $\overline{Q_{s,s}}^{(2,2)}$ is collision integral for s – s colliding pairs (average collision cross-section) (m²), which is the average over a Maxwellian distribution of the collision cross-section for the s – s colliding pairs (m²) [54].

As expressed in Eq. (53), the accuracy of the viscosity is dependent on the $\overline{Q_{s,s}}^{(2,2)}$, whose values are usually presented in a tabulated form. For improved computational efficiency, various curve-fitting formulas are proposed such as the Gupta [51], Palmer [88], and Capitelli models [89]. The Gupta and Palmer curve-fitting models were derived from the same collision integral data. The Gupta and Capitelli models are expressed in Eq. (54) [51] and Eq. (55) [89], respectively.

$$\overline{Q_{s,r}}^{(2,2)} = \exp(D) T^{(A(\ln T)^2 + B \ln T + C)}. \tag{54}$$

$$\overline{Q_{s,r}}^{(2,2)} = \frac{a_1 + a_2 T^{a_3}}{a_4 + a_5 T^{a_6}} \text{ for heavy particles - heavy particles,}$$

$$\overline{Q_{s,r}}^{(2,2)} = \frac{a_3 (\ln T)^{a_6} \exp[(\ln T - a_1)/a_2]}{\exp[(\ln T - a_1)/a_2] + \exp[-(\ln T - a_1)/a_2]} + a_7 \exp\{-[(\ln T - a_8)/a_9]^2\} + a_4 [1 + (\ln T)^{a_5}] \text{ for electron - heavy particles.} \tag{55}$$

Another widely used method for calculating the viscosity of individual species is the curve-fitting method, in which the viscosity is a function of the temperature. These include the Blottner model [90] and Gupta model [51] presented in Eqs. (56) and (57), respectively.

$$\mu_s = 0.1 \times \exp((A_B \ln(T) + B_B) \ln(T) + C_B). \tag{56}$$

$$\mu_s = 0.1 \times [\exp(C_G)] T^{[A_G \ln T + B_G]}. \tag{57}$$

The above numerical models for calculating the viscosity considers only one temperature. It is indisputable that T is the temperature of the flow field in the one-temperature model. However, for two- or three-temperature models, T is generally defined as the translational temperature [18, 51].

5.4.3 Thermal conductivities of individual species

Based on the kinetic theory, the translational thermal conductivity of the heavy species s is expressed as [51]

$$\kappa_{t,s} = \frac{75}{64} \frac{k \sqrt{\pi kT/m_s}}{Q_{s,s}^{(2,2)}} = \frac{15}{4} \mu_s R_s = 1.5 \mu_s C p_{t,s} = 2.5 \mu_s C v_{t,s}. \tag{58}$$

The internal thermal conductivity resulting from the diffusion of the internal excitation energy of the species s is written as [51, 88, 91]

$$\kappa_{int,s} = \frac{3}{8} \frac{C p_{int,s}}{R_s} \frac{k \sqrt{\pi kT/m_s}}{Q_{s,s}^{(1,1)}} = \mu_s C p_{int,s} \left(\frac{\rho_s D_{s,s}}{\mu_s} \right) = \mu_s C p_{int,s} \frac{1}{Sc_{s,s}}, \tag{59}$$

where $D_{s,s}$ is the self-diffusion coefficient, and Sc is the Schmidt number.

According to Eq. (59), the rotational, vibrational, and electronic thermal conductivities of species s can be written as

$$\kappa_{r,s} = \mu_s C v_{r,s} \frac{1}{Sc_{s,s}}, \quad \kappa_{v,s} = \mu_s C v_{v,s} \frac{1}{Sc_{s,s}}, \quad \kappa_{el,s} = \mu_s C v_{el,s} \frac{1}{Sc_{s,s}}. \tag{60}$$

For the one-temperature model, the total thermal conductivity consists of the translational thermal conductivity (κ_t) and internal thermal conductivity (κ_{int}) written as

$$\kappa_s = \kappa_{t,s} + \kappa_{int,s}. \tag{61}$$

For the two-temperature model, the translational-rotational ($\kappa_{tr,s}$) and vibrational-electron-electronic ($\kappa_{ve,s}$) thermal conductivities of the heavy species s are written as

$$\kappa_{tr,s} = \kappa_{t,s} + \kappa_{r,s}, \tag{62}$$

$$\kappa_{ve,s} = \kappa_{v,s} + \kappa_{el,s}. \tag{63}$$

For the three-temperature model, the translational-rotational thermal conductivity $\kappa_{tr,s}$ is given by Eq. (62). The vibrational ($\kappa_{v,s}$) and electronic thermal ($\kappa_{el,s}$) conductivities are expressed in Eq. (60).

5.4.4 Mixing rules

For a mixture, the viscosity and thermal conductivity in each energy mode can be calculated by individual species quantities with appropriate mixing rules. In the 1950s, Wilke’s mixing rule [92] was developed by simplifying the full first-order Chapman–Enskog relation. This mixing rule sets the collision integral ratio as 5/3, and assumes that all binary interactions have the same cross-section [93]. The mixture viscosity and thermal conductivity in each energy mode with Wilke’s mixing rule are expressed as follows [94]:

$$Q = \sum_s \frac{Q_s X_s}{\phi_s}, \tag{64}$$

where Q represents the viscosity (μ) and thermal conductivity ($\kappa, \kappa_{tr}, \kappa_{ve}, \kappa_v, \kappa_{el}$) quantities, X is the molar fraction, and ϕ_s is a scaling factor, defined as

$$\phi_s = X_s + \sum_{r \neq s} X_r \left[1 + \sqrt{\frac{\mu_s}{\mu_r}} \left(\frac{M_r}{M_s} \right)^{1/4} \right]^2 \left[\sqrt{8 \left(1 + \frac{M_s}{M_r} \right)} \right]^{-1}. \tag{65}$$

However, Wilke’s mixing rule is only applicable to neutral gases, and the environmental temperature is limited to 10,000 K. Armaly and Sutton [95] proposed a mixing rule for partially ionized gas mixtures, in which different types of particle interactions are considered to obtain a more accurate approximation of the multicomponent transport properties. The ϕ_s is expressed as [95]

$$\phi_s = X_s + \sum_{r \neq s} X_r \left[\frac{5}{3\mathcal{A}_{s,r}^*} + \frac{M_r}{M_s} \right] \left[1 + \frac{M_r}{M_s} \right]^{-1} \left[\mathcal{F}_{s,r} + \mathcal{B}_{s,r} \sqrt{\frac{\mu_s}{\mu_r}} \left(\frac{M_r}{M_s} \right)^{1/4} \right]^2 \left[\sqrt{8 \left(1 + \frac{M_s}{M_r} \right)} \right]^{-1}, \tag{66}$$

where the coefficients \mathcal{A}^* , \mathcal{B} , and \mathcal{F} depend on the type of particle interaction. The recommend value of \mathcal{A}^* is 1.1 for the interactions between atom and its own ion, and 1.25 for other interactions [93]. \mathcal{B} is recommended the value of 0.78 for the neutral–neutral interactions, 0.15 for the neutral-ion interactions, and 1.0 for the ion-ion, ion–electron, and electron–electron interactions [93]. \mathcal{F} is usually assumed equal to 1.0 for all interactions [93].

5.4.5 Viscosity and thermal conductivities of a mixture based on collision integrals

Gupta [51] and Gnoffo [71] used collision integrals to directly calculate the mixture viscosity and thermal conductivity of weakly ionized flows. Because the interactions of each collision pair in a multicomponent mixture are considered, this model is more physically accurate than mixing rule models that use an approximation of the Chapman–Enskog formula [88].

The calculation of the collision terms among the heavy species is based on the translational temperature T_p , whereas that between electrons and other species is based on the electron temperature T_e [71]. The mixture viscosity calculated by collision integrals is expressed as [51, 71]

$$\mu = \sum_{s \neq e} \left[\frac{m_s X_s}{\sum_{r \neq e} X_r \Delta_{s,r}^{(2)}(T_t) + X_e \Delta_{s,e}^{(2)}(T_e)} \right] + \frac{m_e X_e}{\sum_r X_r \Delta_{e,r}^{(2)}(T_e)}. \tag{67}$$

The translational (κ_t), rotational (κ_r), vibrational (κ_v), electronic excitation (κ_{el}), and electron translation (κ_e) thermal conductivities of the mixture are defined in Eqs. (68)–(72) [51].

$$\kappa_t = \frac{15}{4} k \sum_{s \neq e} \frac{X_s}{\sum_{r \neq e} \alpha_{s,r} X_r \Delta_{s,r}^{(2)}(T_t) + 3.54 X_e \Delta_{s,e}^{(2)}(T_e)}, \tag{68}$$

$$\kappa_r = k \sum_{s=mol} \frac{X_s}{\sum_{r \neq e} X_r \Delta_{s,r}^{(1)}(T_t) + X_e \Delta_{s,e}^{(1)}(T_e)}, \tag{69}$$

$$\kappa_v = k \sum_{s=mol} \frac{(Cp_{v,s}/R_s)X_s}{\sum_{r \neq e} X_r \Delta_{s,r}^{(1)}(T_t) + X_e \Delta_{s,e}^{(1)}(T_e)}, \tag{70}$$

$$\kappa_{el} = k \sum_{s=mol} \frac{(Cp_{el,s}/R_s)X_s}{\sum_{r \neq e} X_r \Delta_{s,r}^{(1)}(T_t) + X_e \Delta_{s,e}^{(1)}(T_e)}, \tag{71}$$

$$\kappa_e = \frac{15}{4} k \frac{X_e}{\sum_{r \neq e} 1.45 X_r \Delta_{e,r}^{(2)}(T_e) + X_e \Delta_{e,e}^{(2)}(T_e)}, \tag{72}$$

where the $\alpha_{s,r}$ is defined as [71, 88]

$$\alpha_{s,r} = 1 + \frac{(1 - M_s/M_r)(0.45 - 2.54M_s/M_r)}{(1 + M_s/M_r)^2}, \tag{73}$$

where $\Delta_{s,r}^{(1)}$ and $\Delta_{s,r}^{(2)}$ are the collision terms ($m \cdot s$) of the heavy species s and r , respectively. These can be calculated by the related collision integrals defined as [71]

$$\Delta_{s,r}^{(1)}(T) = \frac{8}{3} \left[\frac{2M_s M_r}{\pi \mathcal{R} T (M_s + M_r)} \right]^{1/2} \overline{Q}_{s,s}^{(1,1)}, \tag{74}$$

$$\Delta_{s,r}^{(2)}(T) = \frac{16}{5} \left[\frac{2M_s M_r}{\pi \mathcal{R} T (M_s + M_r)} \right]^{1/2} \overline{Q}_{s,s}^{(2,2)}. \tag{75}$$

According to Eq. (67) and Eqs. (68)–(72), the mixture viscosity and thermal conductivities of different master equations can be easily obtained by replacing the corresponding control temperature in the collision terms. For the one-temperature model, both the heavy-species translation temperature T_t and electron translational temperature T_e can be replaced by the temperature T . For the two-temperature model, T_t and T_e should be replaced by the translational-rotational temperature T_{tr} and vibrational-electron-electronic temperature T_{ve} , respectively. For the three-temperature model, T_t and T_e should be replaced by T_{tr} and the electron-electronic temperature T_{el} , respectively.

5.4.6 Species diffusion

Accurate knowledge of the species diffusion in multicomponent gas mixtures is important for predicting surface properties, especially the surface heat transfer. Four models can be used to calculate the mass diffusion flux $J_{s,j}$: the Fick model, Modified Fick model, Self-consistent effective binary diffusion (SCEBD) model, and Stefan–Maxwell model.

The mass diffusion flux is proportional to the gradient of the mass fraction of the heavy species s based on the Fick model written as [96]

$$J_{s \neq e, j} = -\rho D_s \frac{\partial Y_s}{\partial x_j}, \tag{76}$$

where Y_s is the mass fraction of species s , and D_s is the effective diffusion coefficient of species s .

The electron mass diffusion flux is calculated by assuming ambipolar diffusion to ensure the charge neutrality of the flow. This is given by [96]

$$J_{e, j} = -\frac{1}{q_e} \sum_{s \neq e} q_s J_{s, j}, \tag{77}$$

where q_s is the charge per unit mass of species s .

To ensure that the sum of the mass diffusion fluxes is zero, Modified Fick model was proposed. The mass diffusion flux of the heavy species s is written as [94]

$$J_{s \neq e, j} = -\rho D_s \frac{\partial Y_s}{\partial x_j} - Y_s \sum_{r \neq e} (-\rho D_r \frac{\partial Y_r}{\partial x_j}). \tag{78}$$

The SCEBD model was developed for multicomponent plasma flows. It uses small electron mass approximation to simplify the mass diffusion flux equations. The mass diffusion flux of the heavy species s is expressed as [97]

$$J_{s \neq e, j} = -\frac{\rho M_s D_s}{RT_{tr}} \frac{\partial (p_s/p)}{\partial x_j} + Y_s \sum_{r \neq e} \frac{\rho M_r D_r}{RT_{tr}} \frac{\partial (p_r/p)}{\partial x_j} + \frac{1}{RT_{tr}} \left[M_s q_s \rho_s D_s - Y_s \sum_{r \neq e} M_r q_r \rho_r D_r \right] E, \tag{79}$$

where M_s and M_r are the molar weights of the species s and r , respectively. The electric field E is defined as

$$E = \frac{p}{q_e \rho_e} \frac{\partial (p_e/p)}{\partial x_j}. \tag{80}$$

The Stefan–Maxwell model was derived by solving the mole fraction gradient. The mass diffusion flux in terms of the mass fraction gradient is expressed as [98]

$$J_{s, j} = -\rho D_s \frac{\partial Y_s}{\partial x_j} + \frac{Y_s}{(1 - X_s)} D_s \sum_{r \neq s} \left(\rho \frac{M}{M_r} \frac{\partial Y_r}{\partial x_j} + \frac{M}{M_r} \frac{J_r}{D_{s,r}} \right). \tag{81}$$

Equation (81) can be solved by an iterative method. First, the mass flux of each heavy species s is calculated at iteration N by [94]

$$J_{s \neq e, j}^N = -\rho D_s \frac{\partial Y_s}{\partial x_j} + \frac{Y_s}{(1 - X_s)} D_s \sum_{r \neq s, e} \left(\rho \frac{M}{M_r} \frac{\partial Y_r}{\partial x_j} + \frac{M}{M_r} \frac{J_r^{N-1}}{D_{s,r}} \right), \tag{82}$$

then the entire set is corrected to iteration $N + 1$ using the closure equation [94]

$$J_{s \neq e, j}^{N+1} = J_s^N - Y_s \sum_{r \neq e} J_r^N. \tag{83}$$

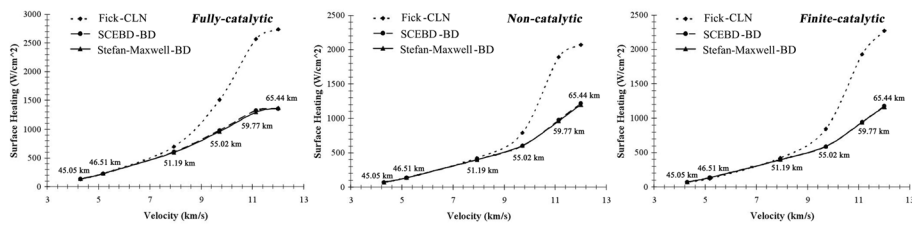


Fig. 11 Heat transfer at the stagnation point of a sphere with different diffusion models [99]

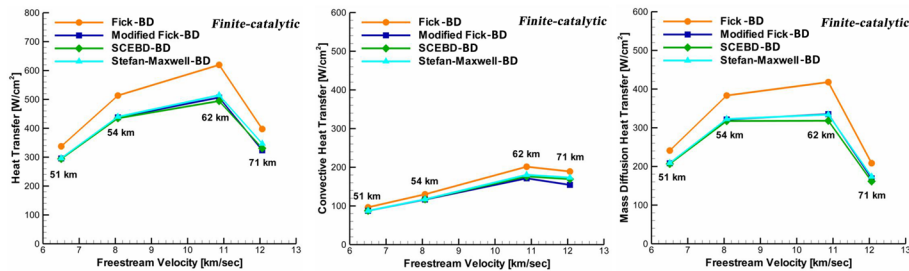


Fig. 12 Total, convective, and diffusion heat transfers at the stagnation point of the Stardust Sample Return Capsule with different diffusion models [94]

In the four diffusion models mentioned above, the effective diffusion coefficient of species s in a mixture D_s can be derived from two numerical models. The first is the constant Lewis number model (CLN), in which a single diffusion coefficient is applied to all species. It is widely used in multicomponent flows consisting of species with similar diffusion properties [18]. In the one-temperature model, the effective diffusion coefficient is written as [99]

$$D_s = D = \frac{\kappa Le}{\rho C_p}, \tag{84}$$

and in the two- and three-temperature models, it is expressed as [94]

$$D_s = D = \frac{\kappa_{tr} Le}{\rho C_{p_{tr}}}, \tag{85}$$

where Le is the Lewis number and usually set to 1.4.

The second model is the binary diffusion (BD) model in which D_s is defined as a function of the binary diffusion coefficient as follows [98]:

$$D_s = (1 - X_s) \left(\sum_{r \neq s} \frac{X_r}{D_{s,r}} \right)^{-1}, \tag{86}$$

where $D_{s,r}$ is the binary diffusion coefficient of the interactions of the heavy species s and r , which can be directly calculated by the collision terms written as [94]

$$D_{s,r} = \frac{kT_t}{p \Delta_{s,r}^{(1)}(T_t)}, \quad s, r \neq e. \tag{87}$$

For the interactions between electrons and other particles, the binary diffusion coefficient $D_{e,r}$ is expressed as

$$D_{e,r} = \frac{kT_e}{p\Delta_{e,r}^{(1)}(T_e)}, \tag{88}$$

where T_t is the translational temperature, which should be replaced by T in the one-temperature model, and by T_{tr} in the two- and three-temperature models. T_e is the electron temperature, which should be replaced by T , T_{ve} , and T_{ele} in the one-, two-, and three-temperature models, respectively.

Gosse [99] compared the surface heat transfers over a sphere with a diameter of 0.23 m calculated by the constant Lewis number Fick diffusion model with those calculated by the binary diffusion SCEBD model and binary diffusion Stefan–Maxwell model. As shown in Fig. 11, the surface heat transfers predicted by the binary diffusion SCEBD and binary diffusion Stefan–Maxwell models are lower than those calculated by the constant Lewis number Fick model. Alkandry [94] investigated the performance of the Fick, modified Fick, SCEBD, and Stefan–Maxwell models with a BD model on the total, convective, and diffusion heat transfers over the Stardust Sample Return Capsule. The finite catalytic wall condition was applied. The results showed that the heat transfer predicted by the Fick model is higher than that predicted by the other models. The heat transfer values calculated by the modified Fick, SCEBD, and Stefan–Maxwell models with the BD model are in good agreement, as shown in Fig. 12.

5.5 Energy transfers

In the thermal nonequilibrium flow, the total energy is the sum of various energies that can exchange with each other. As shown in the conservation equations of the vibrational-electronic energy, vibrational energy, and electron energy (Eqs. (20)–(22)), the source terms Q_v , Q_e , and Q_{ve} are expressed as [70]

$$Q_v = \sum_{s=mol} Q_{s,V-T} + \sum_{s=mol} Q_{s,e-V} + \sum_{s=mol} Q_{s,C-V}, \tag{89}$$

$$Q_e = \sum_{s \neq e} Q_{s,T-e} + Q_{e,C-e} - \sum_{s=mol} Q_{s,e-V} + \sum_{s=ion} Q_{s,e-i}, \tag{90}$$

$$Q_{ve} = \sum_{s=mol} Q_{s,V-T} + \sum_{s=mol} Q_{s,C-V} + \sum_{s \neq e} Q_{s,T-e} + Q_{e,C-e} + \sum_{s=ion} Q_{s,e-i}, \tag{91}$$

where $Q_{s,V-T}$ is the energy transfer between vibrational and translational modes, $Q_{s,e-V}$ is the energy transfer due to inelastic collisions between electron and molecules, $Q_{s,C-V}$ is the energy lost/gained due to the molecular depletion/production, $Q_{s,T-e}$ is the energy transfer due to the elastic collision between electrons and heavy particles, $Q_{e,C-e}$ is the electronic energy lost/gained due to the electronic depletion/production, and $Q_{s,e-i}$ is the energy transfer due to the electron impact ionization.

5.5.1 Vibrational-translational energy transfer

Two formulas can be used to calculate the energy exchange between the translational and vibrational energy modes ($Q_{s,V-T}$): the classical Landau–Teller formula and modified Landau–Teller formula [100] given by Eqs. (92) and (93), respectively. Compared with the classical Landau–Teller formula, the modified Landau–Teller formula can be used in a strong nonequilibrium environment, such as the arbitrary deviation from the thermal equilibrium [101].

$$Q_{s,V-T} = \rho_s \frac{e_{v,s}(T_t) - e_{v,s}(T_v)}{\tau_{s,V-T}} = \rho_s \frac{Cv_{v,s}(T_t - T_v)}{\tau_{s,V-T}}, \tag{92}$$

$$Q_{s,V-T} = \frac{T_t}{T_v} (T_t - T_v) \rho_s \frac{Cv_{v,s}}{\tau_{s,V-T}}, \tag{93}$$

where $\tau_{s,V-T}$ is the average relaxation time between the translational and vibrational energies of molecule s . For a mixture, $\tau_{s,V-T}$ is given by

$$\tau_{s,V-T} = \frac{\sum_{r=mol} X_r}{\sum_{r=mol} X_r / \tau_{s-r,V-T}}. \tag{94}$$

Millikan and White proposed a semi-empirical model, the M-W formula, to evaluate the V-T relaxation time between species s and r ($\tau_{s-r,V-T}$). However, this formula is linearly dependent on the $T_{tr}^{-1/3}$, which results in the underestimation of the V-T relaxation times at high temperatures [102]. Thus, a series of correction methods based on the Millikan–White model have been proposed. The most widely used method is Park’s correction, which takes into account the inaccurate estimation of the collision cross-sections at high temperatures. The model of the Millikan–White formula with Park’s correction is called the M-W–P model written as [16]

$$\tau_{s-r,V-T} = \tau_{s-r,V-T}^{MW} + \tau_{s-r,V-T}^P, \tag{95}$$

with

$$\tau_{s-r,V-T}^{MW} = \frac{1}{p} \exp \left[A_{s,r} \left(T_{tr}^{-1/3} - B_{s,r} \right) - 18.42 \right] \tag{96}$$

and

$$\tau_{s-r,V-T}^P = \frac{1}{\bar{c}_s \sigma_{v,s} n_{s,r}}, \tag{97}$$

where the unit of p is atm. The coefficients $A_{s,r}$ and $B_{s,r}$ can be calculated by the expressions [16] in Eqs. (98) and (99); \bar{c}_s is the average molecular speed (m/s) defined as $\sqrt{8RT/\pi M_s}$; $n_{s,r}$ is the number density of the colliding pair of species s and r (m^{-3}); and $\sigma_{v,s}$ is the limited collision cross-section (m^2) calculated by Eq. (100).

$$A_{s,r} = 1.16 \times 10^{-9/2} \sqrt{\frac{M_s M_r}{M_s + M_r}} \theta_{v,s}^{4/3}, \quad (98)$$

$$B_{s,r} = 0.015 \times 10^{-3/4} \left(\frac{M_s M_r}{M_s + M_r} \right)^{1/4}, \quad (99)$$

$$\sigma_{v,s} = \sigma'_{v,s} (50000/T)^2, \quad (100)$$

where the values of $\sigma'_{v,s}$ for N_2 , O_2 , and NO are usually set as $3 \times 10^{-21} \text{ m}^2$ [16].

Schwartz et al. proposed a more quantitative calculation model of the V-T relaxation time called the S-S-H model [103], which considers the probability of energy transfer between the vibrational energy and translational energy. The V-T relaxation time $\tau_{s-r,V-T}$ is related to the probability P_{10} of $1 \rightarrow 0$ transitions by the Landau-Teller relation [104].

$$\tau_{s-r,V-T} = \frac{1}{Z P_{10} (1 - e^{-h\omega/kT})}, \quad (101)$$

where Z is the number of collisions a molecule experiences per second, h is the Planck's constant, and ω is the frequency of the transition $1 \rightarrow 0$.

The probability P_{10} can be derived from the rate coefficient k_{10} (cm^3/s) for the deactivation of the lowest excited vibrational level. The related expression is written as

$$P_{10} = k_{10} \left(2d_{s,r}^2 \sqrt{\frac{2\pi kT}{m_{s,r}}} \right)^{-1}, \quad (102)$$

where $d_{s,r}$ is the collision diameter, and $m_{s,r}$ is the reduced mass of the colliding pairs s and r .

The rate coefficient of the specific colliding pair is expressed as an approximation based on the experimental data.

$$k_{10} = AT^n \exp \left\{ -\frac{B}{T^{1/3}} + \frac{C}{T^m} \right\} \times \left[1 - D \times \exp \left\{ -\frac{E_{10}}{T} \right\} \right]^{-1}, \quad (103)$$

where the recommended values of the parameters n , m , A , B , C , and D are referred to reference [104].

However, both the M-W-P and S-S-H models of the V-T relaxation time are simplified models that do not consider the reactive interactions. Recently, a kinetic model based on the rigorous kinetic theory of the V-T relaxation time was discussed as integrals of the relative velocity and scattering angles of the vibrational quantum obtained/lost during the elementary V-T transition [100]. Kustova [102, 105] derived a detailed calculation process of the V-T relaxation time with this model. Oblapenko [106] calculated the V-T relaxation times of N_2 , O_2 , and NO in collisions with air species with this model and compared the results with those of the M-W model, experimental data, and quasi-classical trajectory calculations (QCT). The comparison showed that the results of the

rigorous-kinetic model of the V-T relaxation time is consistent with the QCT and experimental data, both quantitatively and qualitatively, over a wide temperature range.

The rigorous-kinetic model of the V-T relaxation time of the collisions between molecules s and particles r is given by

$$\tau_{s-r,V-T} = \left[\frac{4kn}{m_s C v_s} \left\langle (\Delta \mathcal{E}_s^v)^2 \right\rangle_{s-r,V-T} \right]^{-1}, \tag{104}$$

where n is the number density of the mixture (m^{-3}), m_s is the mass of species s (kg/particle), $C v_s$ is the specific vibrational heat of species s , $\Delta \mathcal{E}_s^v$ is the reduced vibrational energy of species s and is defined as $\Delta \mathcal{E}_s^v = (\varepsilon_s^{i'} - \varepsilon_s^i)/kT$, in which i and i' denote the vibrational levels of species s before and after the V-T transition, respectively.

5.5.2 Chemical-vibrational energy transfer

The internal energies contribute to overcoming the activation threshold of chemical reactions; therefore, molecules in higher vibrational states are more likely to dissociate [107]. Figure 13 shows the relationship between the vibrational energy at various states and the energy required for the dissociation of diatomic molecules. The total energy required for molecular dissociation is denoted by ε_d , while the vibrational energy at the level i state is denoted by ε_v^i . The energy ($\Delta \varepsilon$) required for dissociation decreases as the vibrational energy level increases. This indicates that the vibrational energies and chemical reaction processes are coupled with each other. Coupled chemical-vibrational models have been proposed for calculating the chemical-vibrational energy exchange rate $Q_{s,C-V}$. These include the Park model [108], Macheret–Fridman model [109], and coupled vibration-dissociation-vibration (CVDV) model [110].

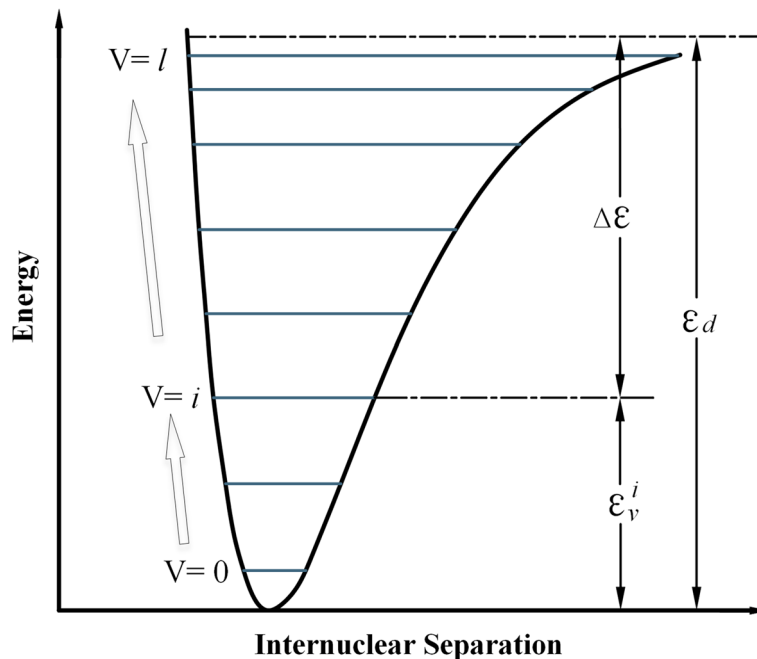


Fig. 13 Schematic of the coupled vibration-dissociation of a molecule [111, 112]

In the Park model, $Q_{s,C-V}$ is the vibrational energy gained or removed by the dissociation reactions of the diatomic molecule s , which is expressed as [108]

$$Q_{s,C-V} = \dot{w}_s \hat{D}_s, \quad (105)$$

where \hat{D}_s denotes the vibrational energy per unit mass of the diatomic molecule s (J/kg), which can be calculated by the preferential model for molecules at higher vibrational energy levels and the non-preferential model for other molecules, written as Eqs. (106) and (107), respectively [18].

$$\hat{D}_s = \alpha_s \varepsilon_{d,s}, \quad (106)$$

$$\hat{D}_s = e_{v,s}, \quad (107)$$

where $\varepsilon_{d,s}$ is the dissociation energy/potential of molecule s ; α_s is a constant usually set as 0.3 [111]; and $e_{v,s}$ is the average vibrational energy of molecule s .

Macheret and Fridman developed a semi-empirical model for homonuclear molecules based on the assumption of impulsive collisions. Taking into account two dissociation regimes stemming from the upper and lower vibrational states, the $Q_{s,C-V}$ is expressed as [113]

$$Q_{s,C-V} = (\dot{w}_{s,b} E_{b,s} - \dot{w}_{s,f} E_{f,s}), \quad (108)$$

where E_f and E_b are the forward and backward weighted average vibrational energy, respectively, expressed as [109]

$$E_{f,s} = (Z_{l,s} \alpha k \theta_{d,s} (T_v/T_a)^2 + Z_{h,s} k \theta_{d,s}) / Z_{M-F,s}, \quad (109)$$

$$E_{b,s} = (1 - L + \alpha L) k \theta_{d,s}, \quad (110)$$

with

$$Z_{M-F,s} = Z_{l,s} + Z_{h,s}, \quad (111)$$

$$Z_{l,s} = L \times \exp \left[-\theta_{d,s} \left(\frac{1}{T_a} - \frac{1}{T_t} \right) \right], \quad (112)$$

$$Z_{h,s} = \frac{1 - \exp(-\theta_{v,s}/T_v)}{1 - \exp(-\theta_{v,s}/T_t)} (1 - L) \times \exp \left[-\theta_{d,s} \left(\frac{1}{T_v} - \frac{1}{T_t} \right) \right], \quad (113)$$

$$\alpha = \left(\frac{m_s}{m_s + m_r} \right)^2, \quad (114)$$

where Z_{M-F} , Z_b and Z_h denote the nonequilibrium factors, θ_v is the characteristic vibrational temperature, θ_d is the characteristic dissociation temperature, L depends on the type of collision pairs, and T_a is the average temperature defined as

$$T_a = \alpha T_v + (1 - \alpha) T_t. \tag{115}$$

The CVDV model is another popular model used to describe the removal of the preferential energy from the upper vibrational energy states via dissociation. It assumes that the dissociation probability is exponentially related to the vibrational energy level. The $Q_{s,C-V}$ is expressed as [110]

$$Q_{s,C-V} = \dot{w}_{b,s} \bar{E}(-U) - \dot{w}_{f,s} \bar{E}(T_F), \tag{116}$$

where $\bar{E}(-U)$ and $\bar{E}(T_F)$ are the weighted average vibrational energies gained by recombination and removed by dissociation, respectively. Both can be simplified by the assumption of truncated harmonic oscillators [113] written as

$$\bar{E}(T) = \frac{k\theta_{v,s}}{\exp(\theta_{v,s}/T) - 1} - \frac{k\theta_{d,s}}{\exp(\theta_{d,s}/T) - 1}. \tag{117}$$

The relation of T_F and U is defined by

$$\frac{1}{T_F} = \frac{1}{T_v} - \frac{1}{T_t} - \frac{1}{U}. \tag{118}$$

If the CVDV model is adopted, then the forward rate coefficient k_f in Eq. (24) should be replaced by [18]

$$k_f = \frac{Z(T_t)Z(T_F)}{Z(T_v)Z(-U)} A_f \times T_{c,f}^{B_f} \exp\left(-\frac{T_a}{T_{c,f}}\right). \tag{119}$$

5.5.3 Other energy transfers

The energy exchange between the vibrational and electronic energy modes $Q_{s,e-V}$ can also be expressed by the classical Landau–Teller formula as

$$Q_{s,e-V} = \rho_s \frac{e_{v,s}(T_e) - e_{v,s}(T_v)}{\tau_{s,e-V}} = \rho_s \frac{Cv_{v,s}(T_e - T_v)}{\tau_{s,e-V}}, \tag{120}$$

where $\tau_{s,e-V}$ is the relaxation time of the vibrational-electronic energy exchange, which is usually given in a tabular form [13].

The energy transfer due to elastic collisions between electrons and heavy particles Q_{s,T_e} is expressed as [71]

$$Q_{s,T-e} = 3\rho_e \mathcal{R}(T_t - T_e) \frac{\nu_{e,s}}{M_s}, \tag{121}$$

where $\nu_{e,s}$ is the effective collision frequency between an electron and the heavy species s written as

$$\nu_{e,s} = \frac{8}{3} \left(\frac{\pi}{m_e}\right)^{1/2} n_s e^4 \frac{1}{(2kT_e)^{3/2}} \ln\left(\frac{k^3 T_e^3}{\pi n_e e^6}\right), \tag{122}$$

where n represents the number density, and e is the electronic charge.

The energy loss due to electron-impact ionization $Q_{s,e-i}$, in which free electrons strike neutral particles and produce ions and electrons, is expressed as [71]

$$Q_{s,e-i} = \dot{w}_s^e \hat{I}_s, \quad (123)$$

where \dot{w}_s^e represents the rate of species s produced by the electron impact ionization reactions ($\text{kg}/(\text{m}^3 \cdot \text{s})$), and \hat{I}_s is the first ionization energy of the species s (J/kg).

The electronic energy increase or loss due to chemical reactions $Q_{s,C-e}$ is written as

$$Q_{e,C-e} = \dot{w}_e e_e. \quad (124)$$

6 Boundary conditions

6.1 Slip boundary conditions

The no-slip boundary conditions commonly used in the CFD method assume that the velocity and temperature of the gas near the wall are equal to those on the wall, and that transport processes near the wall are not affected by wall collisions. However, from a microscopic perspective, the transport of the momentum, heat, and mass of the gas near the wall is not the same as that in the interior of the gas [114]. Hence, the results based on the no-slip assumption are inaccurate for rarefied gas, where the mean free path cannot be ignored [115]. When the mean free path becomes comparable to the characteristic length of the flow, the flow should be treated at the level of a velocity distribution function, such that the kinetic Boltzmann equation or DSMC method [116] is adopted. However, both methods require significant computational effort at a low Kn , which is difficult for practical applications. Therefore, it is important to find ways to expand the application scope of the CFD method. The slip boundary conditions extend the CFD method to moderately rarefied gas. As shown in Fig. 3, the slip boundary conditions extend the application range of the CFD method from $Kn < 0.001$ to $Kn < 0.1$.

Based on the kinetic theory, Maxwell [117] proposed a model for the slip velocity u_s at the solid surface expressed as [118]

$$u_s - u_w = \sigma_p \frac{v_m \mu}{p} \frac{\partial u_x}{\partial n} \Big|_0 + \sigma_T \frac{\mu}{\rho T} \frac{\partial T}{\partial x} \Big|_0, \quad (125)$$

where μ is the shear viscosity; v_m is the most probable speed of the gas, defined as $\sqrt{2kT/m}$; x and n are the Cartesian coordinates in the parallel and normal directions to the solid surface, respectively; and σ_p and σ_T are the viscous and thermal slip coefficients, respectively. The second term on the right-hand side is related to thermal creep; hence, it can be neglected for an isothermal wall. Under the diffuse-specular boundary condition, Maxwell derived the σ_p and σ_T as [118]

$$\sigma_p = \frac{2 - \alpha_M}{\alpha_M}, \quad \sigma_T = \frac{3}{4}, \quad (126)$$

where α_M is the probability of diffuse scattering, and the range of α_M is 0–1.

Based on the analysis of the Maxwell model for momentum slip, Smoluchowski proposed the temperature slip model, which assumes that the energy brought to the

boundary by approaching molecules is responsible for the heat conducted through the boundary [119]. This is expressed as

$$T_s - T_w = \frac{2 - \alpha_T}{\alpha_T} \frac{2\gamma}{(\gamma + 1)Pr} \lambda \left. \frac{\partial T}{\partial n} \right|_0, \tag{127}$$

where α_T is the fraction of molecules reflected by the wall temperature, γ is the ratio of specific heats, and Pr is the Prandtl number. λ is the molecular mean free path defined as [119]

$$\lambda = \frac{\mu}{\rho} \sqrt{\frac{\pi}{2RT}}, \tag{128}$$

where R is the specific gas constant (J/(kg·K)).

In the N-S equations, the shear stress was assumed to vary linearly with the velocity gradient on the wall, where the rarefied flow near the surface was not considered. However, a nonlinear velocity profile and finite slip velocity developed near the surface owing to infrequent gas–gas interactions [120]. This boundary layer with a nonlinear velocity distribution is called the Knudsen layer, with a thickness of several mean free paths of gas molecules. To accurately predict the velocity profile in the Knudsen layer, Lockerby [121] proposed a correction by modeling the local gas viscosity in the Knudsen layer as

$$\mu = \mu / \Psi(n/\lambda), \tag{129}$$

where the “wall-function” $\Psi(n/\lambda)$ is expressed as

$$\Psi(n/\lambda) \approx 1 + 0.7(1 + n/\lambda)^{-3}. \tag{130}$$

The Knudsen layer function is another method to calculate the velocity profile in the Knudsen layer, which describes the relationship between the defect velocity u_d and the normal distance to the surface n . Recently, Su et al. [120] and Wang et al. [118] solved the linearized Boltzmann equation with a diffuse-specular boundary condition to obtain a series of velocities in the Knudsen layer, which were fitted to the Knudsen layer function. The defect velocity u_d , which describes the deviation of the linearly extrapolated velocity in the bulk region from the true velocity [120] inside the Knudsen layer, is defined as [118]

$$\frac{u_d(n)}{u_d(0)} = \sum_{i=0}^2 \sum_{j=0}^2 c_{i,j} n^i (n \ln n)^j, \tag{131}$$

$$u_d(0) = c_1 [1 - \exp(-c_2 \alpha_M)], \tag{132}$$

where $c_{i,j}$, c_1 , and c_2 are the fitting coefficients from [118].

6.2 Catalytic wall

In a hypersonic air flow, a large number of atoms, ions, and electrons are produced around the shock wave owing to the high temperature. These atoms, ions, and electrons

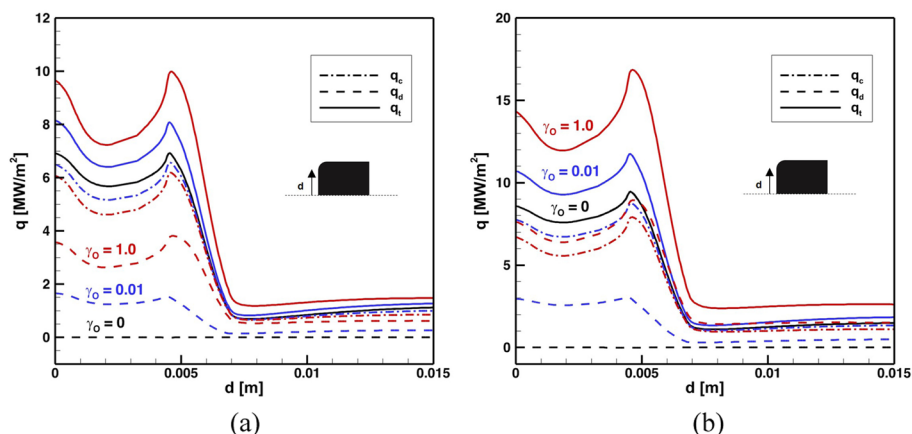


Fig. 14 Heat flux on a calorimeter probe for the mixtures: (a) O₂-Ar and (b) N₂-Ar [132]

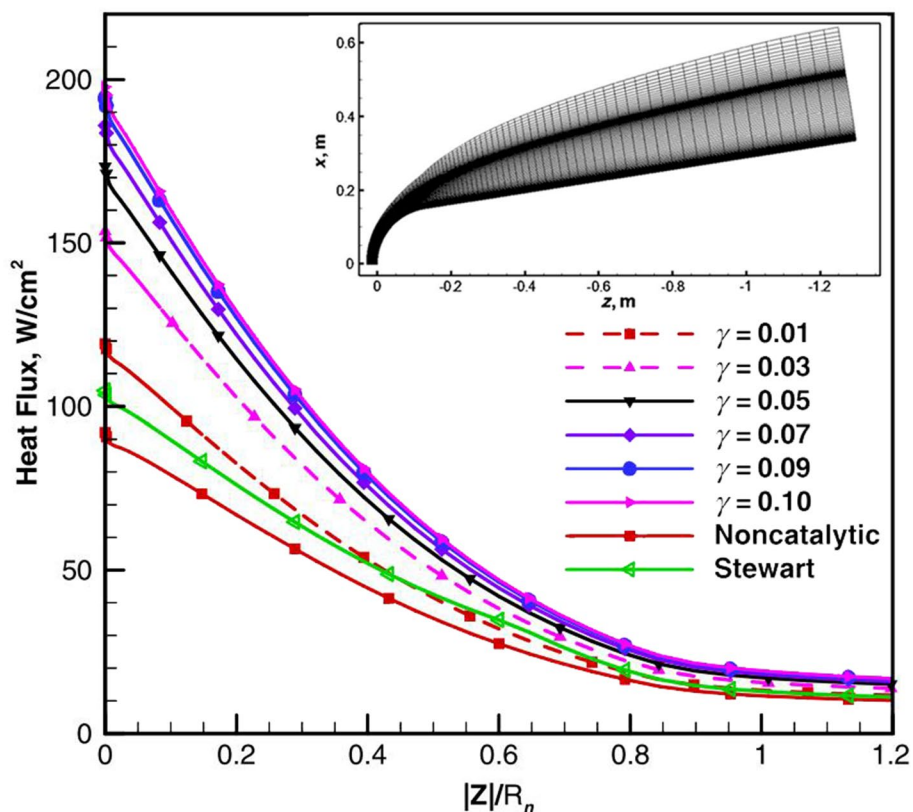


Fig. 15 Heat flux for RAM-C II [132]

recombine into molecules at the surface owing to the low surface temperature. These recombination reactions are exothermic reactions that release heat to the surface, which significantly increases the surface heat flux [122].

In the 1990s, Scott [123] proposed a phenomenological model (global one-step model [124]) for catalytic atom recombination. Scott assumed that the atoms diffused to the surface and were specularly reflected from the surface or completely adsorbed by the

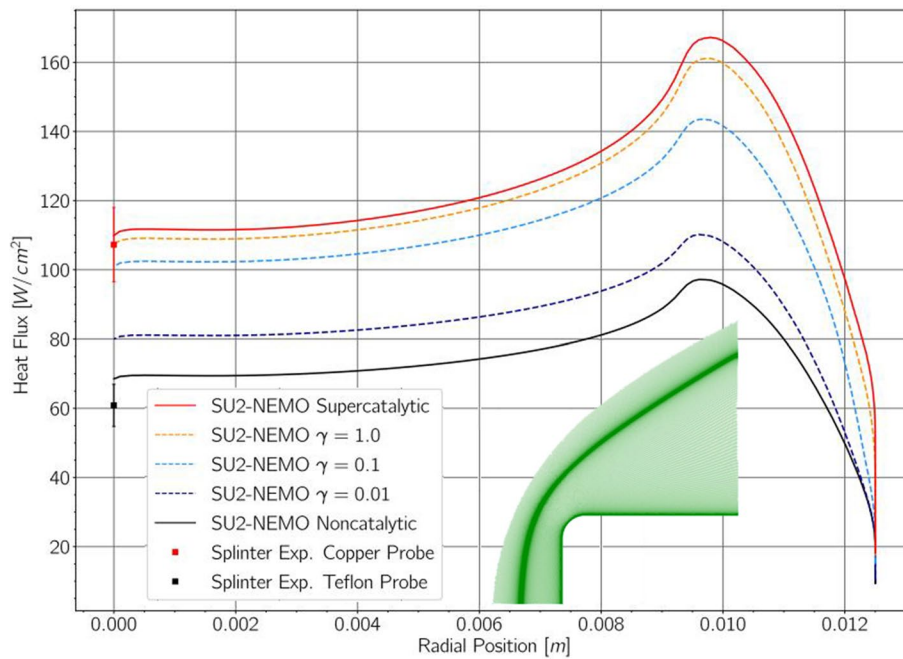


Fig. 16 Heat flux on a calorimeter probe [133]

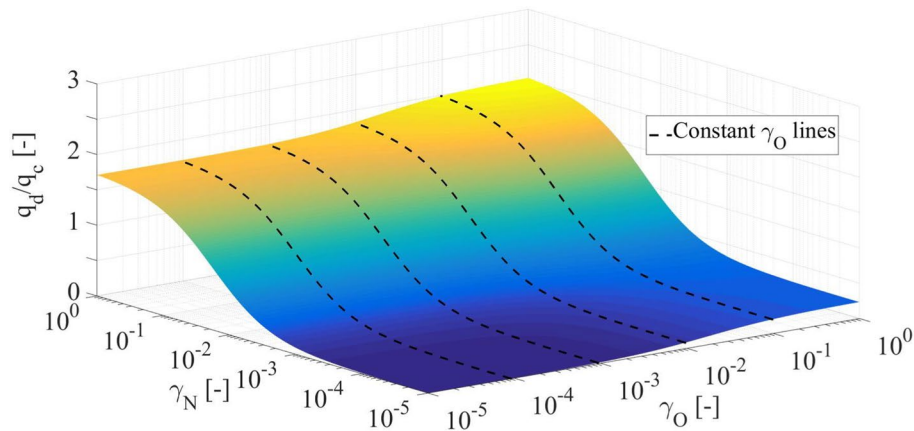


Fig. 17 Surface plot of oxygen and nitrogen catalytic efficiency on the diffusion heat transfer [124]

surface. The recombination coefficient γ_s was proposed to define the ratio of the recombining atoms and the incident atoms impinging on the surface. This is expressed as

$$\gamma_s = \frac{|N_{s,re}|}{|N_{s,tot}|}. \tag{133}$$

The recombination coefficient is limited to the range of 0–1. $\gamma_s = 1$ and $\gamma_s = 0$ denote a fully catalytic and noncatalytic wall, respectively. The value of γ_s is usually obtained experimentally; for related experiment investigations, please refer to [125–127].

Owing to the recombination reactions, the normal component of the net mass flux of atom s consumed on the surface is expressed as

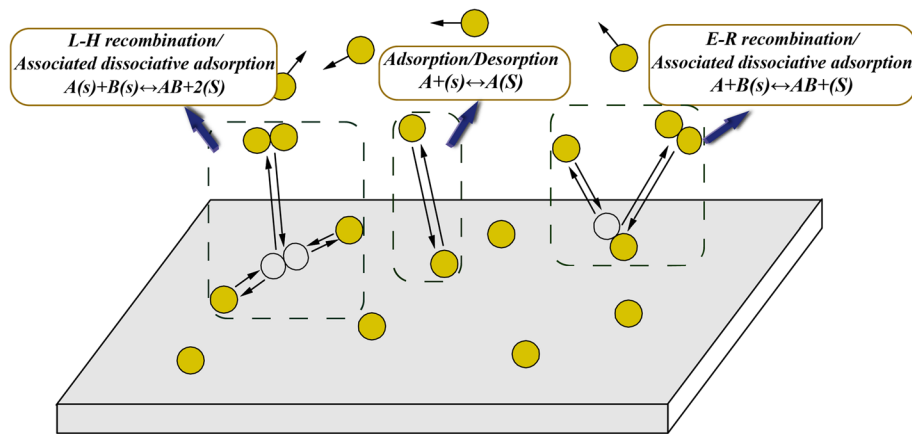


Fig. 18 Mechanisms of catalytic recombination reaction on the surface

$$\dot{m}_s = -k_s(\rho_w Y_{w,s})^P, \tag{134}$$

where P is the chemical order of the reaction (usually set as 1), $Y_{w,s}$ is the mass fraction of atom s on the surface, and k_s is the recombination rate derived from the Hertz–Knudsen relation written as

$$k_s = \gamma_s \sqrt{\frac{kT_w}{2\pi m_s}}. \tag{135}$$

The net mass flux generated by the diffusion of atom s to the surface is given by

$$J_s = \rho_w D_{w,s} \left(\frac{\partial Y_{w,s}}{\partial n} \right). \tag{136}$$

According to the mass balance on the surface, the net mass flux of species s formed at the surface is zero. The mass flux due to the recombination reactions must be balanced by that of the diffusion to the surface [128], which is expressed as

$$\dot{m}_s + J_s = 0. \tag{137}$$

Substituting Eq. (134) and Eq. (136) into Eq. (137) with $P=1$, the final form is written as

$$-k_s \rho_w Y_{w,s} + \rho_w D_{w,s} \left(\frac{\partial Y_{w,s}}{\partial n} \right) = 0. \tag{138}$$

Many related investigations [129–133] have confirmed that catalytic recombination reactions on the wall can significantly increase the aerothermal load on the surface of vehicles. The diffusive heat flux caused by recombination reactions is the main reason for the increasing aerodynamic heat [132], as shown in Fig. 14. The catalytic recombination coefficient plays a significant role in the prediction of the aerodynamic heat. The heat flux increases with the improvement of the catalytic recombination coefficient, as shown in Figs. 15 and 16. However, the heat flux does not continuously increase as the catalytic recombination coefficients increases [133], whereas a strong

sensitivity of the catalytic heating augmentation for weakly and moderately catalytic walls exists [134]. Different catalytic recombination coefficients of different atoms have been considered by Yang and Park [124]. The surface plot of the ratio of the diffusive heat flux and convective heat flux is shown in Fig. 17.

The phenomenological model suffers from oversimplification; it only considers the net effect of the surface and ignores the detailed chemical reaction mechanisms [135]. Moreover, a frozen boundary layer is assumed in this model, in which the timescale of the atomic diffusion to the surface is considered to be much shorter than that of the recombination reactions [127]. Figure 18 shows the three interaction mechanisms between the gas and surface [136, 137], where s denotes the surface and $A(s)$ denotes an atom adsorbed on the surface.

(1) Adsorption/desorption: $A + (s) \leftrightarrow A(s)$.

(2) Eley–Rideal (E–R) recombination/associated dissociative adsorption: $A + B(s) \leftrightarrow AB + (s)$.

(3) Langmuir–Hinshelwood (L–H) recombination/associated dissociative adsorption: $A(s) + B(s) \leftrightarrow AB + 2(s)$.

It can be seen that atoms diffuse near the solid wall, and some of them are directly absorbed by the surface. In the E–R recombination, the atoms in the gas phase directly recombine with the atoms absorbed on the surface to form molecules, which are then desorbed from the surface. In the L–H recombination, the atoms absorbed on the surface recombine with each other, and are then desorbed from the surface in the form of molecules.

Based on the interaction mechanisms presented in Fig. 18, a gas/surface finite-rate model has been proposed and widely discussed [136, 138, 138], which enables the definition of an arbitrary number of physical interactions and chemical reactions between the gas and surface. The mass flux of species s on the surface is defined as

$$\dot{m}_s = M_s \sum_{i=1}^{nr} \left\{ (v''_{si} - v'_{si}) \left(k_{fi} \prod_{s=1}^{ns} [X_s]^{v'_{si}} - k_{bi} \prod_{s=1}^{ns} [X_s]^{v''_{si}} \right) \right\}. \quad (139)$$

This formula is similar to the finite-rate formulation of the gas phase chemistry in Eq. (23) [138]. However, this formula describes the species production/loss on the surface; thus, the unit of the forward and backward rate coefficients is $\text{m}^2/(\text{s}\cdot\text{mole})$.

7 Conclusion

This paper is a primer for readers interested in hypersonic flows. It introduces the physical phenomena inherent in hypersonic flows and the flow characteristics of three types of hypersonic flows (thermochemical equilibrium flow, chemical nonequilibrium flow, and thermochemical nonequilibrium flow). Then, the Kn ranges for applying the CFD method, conventional N–S equations, and nonequilibrium N–S equations are summarized. State-of-the-art mathematical modeling based on the CFD method and related calculation processes for the three hypersonic flows are reviewed in detail.

For the thermochemical equilibrium flow, conventional N–S equations can be used, in which the individual species concentrations are not explicitly required. The calculation accuracy of the aerodynamic parameters is dependent on the inputs of the transport

and thermodynamic properties. Related studies on these properties are summarized in a Table. Three methods for calculating the chemical compositions of the thermochemical equilibrium flow are also reviewed. For the two nonequilibrium flows, the flow equations should be coupled with chemical reactions. Three types of nonequilibrium N-S equations are reviewed: one-, two-, and three-temperature models. The one-temperature model is applied to the chemical nonequilibrium flow, while two- and three-temperature models are applied to the thermochemical nonequilibrium flow. Several chemical kinetic models, derivations of the thermodynamic and transport properties of an individual species or mixture, and numerical models of energy transfers between different energy modes are presented in detail.

Two special wall boundary conditions that frequently appear in hypersonic flows (i.e., slip boundary condition and catalytic wall) are introduced. The corresponding numerical models and application research are reviewed.

Acknowledgements

Not applicable.

Authors' contributions

WZ designed the framework of this paper, and was a major contributor in writing the manuscript. ZZ participated in the design of this paper, and was a major contributor in revising the manuscript. XW revised Section 5.3 (Thermodynamic properties) in the manuscript. TS polished the language of the manuscript. All authors read and approved the final manuscript.

Funding

This research was supported by the Key Laboratory of Hypersonic Aerodynamic Force and Heat Technology of the AVIC Aerodynamics Research Institute, National Natural Science Foundation of China (Grant Nos. 31371873, 31000665, 51176027, and 31300408), Special Program for Applied Research on Super Computation of the NSFC-Guangdong Joint Fund (the second phase) of China and CAST-BISEE (Beijing Institute of Spacecraft Environment Engineering) innovation fund.

Availability of data and materials

Not applicable.

Declarations

Competing interests

The authors declare that they have no competing interests.

Received: 17 June 2022 Accepted: 13 September 2022

Published online: 19 December 2022

References

1. Viviani A, Pezzella G (2015) Basics of hypersonic aerodynamics and aerothermodynamics. In: Aerodynamic and aerothermodynamic analysis of space mission vehicles. Springer Cham, Switzerland
2. Szirczak D, Smith H (2016) A review of design issues specific to hypersonic flight vehicles. *Prog Aerosp Sci* 84:1–28
3. Anderson JD Jr (2006) Hypersonic and high-temperature gas dynamics, 2nd edn. American Institute of Aeronautics and Astronautics Inc, Reston
4. Yang J, Liu M (2019) Numerical analysis of hypersonic thermochemical non-equilibrium environment for an entry configuration in ionized flow. *Chin J Aeronaut* 32(12):2641–2654
5. Gu S, Olivier H (2020) Capabilities and limitations of existing hypersonic facilities. *Prog Aerosp Sci* 113:100607
6. Moreira FC, Wolf WR, Azevedo JLF (2021) Thermal analysis of hypersonic flows of carbon dioxide and air in thermodynamic non-equilibrium. *Int J Heat Mass Transf* 165:120670
7. Schwartzentruber TE, Boyd ID (2015) Progress and future prospects for particle-based simulation of hypersonic flow. *Prog Aerosp Sci* 72:66–79
8. Schouler M, Préveraud Y, Mieussens L (2020) Survey of flight and numerical data of hypersonic rarefied flows encountered in earth orbit and atmospheric reentry. *Prog Aerosp Sci* 118:100638
9. Reinert JD, Candler GV, Komives JR (2020) Simulations of unsteady three-dimensional hypersonic double-wedge flow experiments. *AIAA J* 58(9):4055–4067
10. Holloway ME, Hanquist KM, Boyd ID (2019) Effect of thermochemistry modeling on hypersonic flow over a double cone. Paper presented at the AIAA Scitech 2019 Forum, San Diego, 7–11 January 2019

11. Nusca MJ (1998) Numerical simulation of electromagnetic wave attenuation in nonequilibrium chemically reacting flows. *Comput Fluids* 27(2):217–238
12. Park C (1987) Assessment of two-temperature kinetic model for dissociating and weakly-ionizing nitrogen. *Journal of Thermophysics and Heat Transfer*, 2(1), 8-16
13. Lee JH (1984) Basic governing equations for the flight regimes of aeroassisted orbital transfer vehicles. Paper presented at the 19th thermophysics conference, Snowmass, 25-28 June 1984
14. Scoggins JB, Leroy V, Bellas-Chatzigeorgis G et al (2020) Mutation++: Multicomponent thermodynamic and transport properties for ionized gases in C++. *SoftwareX* 12:100575
15. Zhang W, Zhang Z, Wang X et al (2019) Hypersonic nonequilibrium flow simulations of a hemispherical nose with a counterflowing jet. *Acta Astronaut* 165:388–400
16. Park C (1993) Review of chemical-kinetic problems of future NASA missions, I: earth entries. *J Thermophys Heat Transf* 7(3):385–398
17. Longo JMA, Hannemann K, Hannemann V (2007) The challenge of modeling high speed flows. Paper presented at the 6th EUROSIM congress on modelling and simulation, Ljubljana, 9-13 September
18. Casseau V (2017) An open-source CFD solver for planetary entry. Dissertation, University of Strathclyde
19. Boyd ID, Schwartzentruber TE (2017) Nonequilibrium gas dynamics and molecular simulation. Cambridge University Press, Cambridge
20. Mackey LE, Boyd ID (2019) Assessment of hypersonic flow physics on aero-optics. *AIAA J* 57(9):3885–3897
21. Scanlon TJ, White C, Borg MK et al (2015) Open-source direct simulation Monte Carlo chemistry modeling for hypersonic flows. *AIAA J* 53(6):1670–1680
22. Espinoza D (2018) An open-source hybrid CFD-DSMC solver for high-speed flows. Dissertation, University of Strathclyde
23. Moreno-Ibáñez M, Silber EA, Gritsevich M et al (2018) Verification of the flow regimes based on high-fidelity observations of bright meteors. *Astrophys J* 863:174
24. Nagnibeda E, Kustova E (2009) Non-equilibrium reacting gas flows. Springer Berlin, Heidelberg
25. Bechina AI, Kustova EV (2019) Rotational energy relaxation time for vibrationally excited molecules. *Vestnik St Petersburg Univ Math* 52:81–91
26. Bird GA (1978) Monte Carlo simulation of gas flows. *Annu Rev Fluid Mech* 10(1):11–31
27. Singh N, Schwartzentruber TE (2016) Heat flux correlation for high-speed flow in the transitional regime. *J Fluid Mech* 792:981–996
28. Moss JN, Bird GA (2003) Direct simulation of transitional flow for hypersonic reentry conditions. *J Spacecr Rockets* 40(5):830-843
29. Cercignani C (1988) The Boltzmann equation and its applications. Springer New York, NY
30. Mieussens L (2000) Discrete-velocity models and numerical schemes for the Boltzmann-BGK equation in plane and axisymmetric geometries. *J Comput Phys* 162(2):429–466
31. Xu K, Huang J-C (2010) A unified gas-kinetic scheme for continuum and rarefied flows. *J Comput Phys* 229(20):7747–7764
32. Grad H (1949) On the kinetic theory of rarefied gases. *Commun Pure Appl Math* 2(4):331–407
33. Struchtrup H, Torrilhon M (2003) Regularization of Grad's 13 moment equations: Derivation and linear analysis. *Phys Fluids* 15(9):2668–2680
34. Gu X-J, Emerson DR (2009) A high-order moment approach for capturing non-equilibrium phenomena in the transition regime. *J Fluid Mech* 636:177–216
35. Holman TD, Boyd ID (2011) Effects of continuum breakdown on hypersonic aerothermodynamics for reacting flow. *Phys Fluids* 23(2):027101
36. Boyd ID, Chen G, Candler GV (1995) Predicting failure of the continuum fluid equations in transitional hypersonic flows. *Phys Fluids* 7(1):210–219
37. Wang W-L, Boyd ID (2003) Predicting continuum breakdown in hypersonic viscous flows. *Phys Fluids* 15(1):91–100
38. Bottin B, Vanden Abeele D, Magin TE, Rini P (2006) Transport properties of collision-dominated dilute perfect gas mixtures at low pressures and high temperatures. *Prog Aerosp Sci* 42(1):38–83
39. Kim KH, Rho OH (2000) Navier–Stokes computation of flows in arc heaters. *J Thermophys Heat Transf* 14(2):250–258
40. Bottin B (2000) Thermodynamic properties of arbitrary perfect gas mixtures at low pressures and high temperatures. *Prog Aerosp Sci* 36(7):547–579
41. Gupta RN, Lee K-P, Thompson RA et al (1990) Calculations and curve fits of thermodynamic and transport properties for equilibrium air to 30000 K. NASA Ref Publ NASA-RP-1260
42. Gordon S, McBride BJ (1994) Computer program for calculation of complex chemical equilibrium compositions and applications I. Analysis. NASA Ref Publ NASA-RP-1311
43. Henderson SJ, Menart JA (2008) Equilibrium properties of high-temperature air for a number of pressures. *J Thermophys Heat Transfer* 22(4):718–726
44. Kee RJ, Rupley FM, Miller JA (1989) Chemkin-II: A Fortran chemical kinetics package for the analysis of gas-phase chemical kinetics. Sandia National Lab Tech Rept SAND-89-8009
45. Reynolds WC (1986) The element potential method for chemical equilibrium analysis: Implementation in the interactive program STANJAN, version 3. Stanford Univ Tech Rept
46. McBride BJ, Gordon S (1996) Computer program for calculation of complex chemical equilibrium compositions and applications II. User's manual and program description. NASA Ref Publ NASA-RP-1311
47. Hansen CF (1959) Approximations for the thermodynamic and transport properties of high-temperature air. NASA Tech Rept NASA-TR-R-50
48. Peng TC, Pindroh AL (1962) An improved calculation of gas properties at high temperature: Air. Aero-Space Div, Boeing Co D2-11722
49. Srinivasan S, Tannehill JC (1987) Simplified curve fits for the transport properties of equilibrium air. NASA Cont Rept NASA-CR-178411

50. Srinivasan S, Tannehill JC, Weilmuenster KJ (1987) Simplified curve fits for the thermodynamic properties of equilibrium air. NASA Ref Publ NASA-RP-1181
51. Gupta RN, Yos JM, Thompson RA et al (1990) A review of reaction rates and thermodynamic and transport properties for an 11-species air model for chemical and thermal nonequilibrium calculations to 30000 K. NASA Ref Publ NASA-RP-1232
52. Bacri J, Raffanel S (1987) Calculation of some thermodynamic properties of air plasmas: Internal partition functions, plasma composition, and thermodynamic functions. *Plasma Chem Plasma Process* 7:53–87
53. Bacri J, Raffanel S (1989) Calculation of transport coefficients of air plasmas. *Plasma Chem Plasma Process* 9:133–154
54. Murphy AB (1995) Transport coefficients of air, argon-air, nitrogen-air, and oxygen-air plasmas. *Plasma Chem Plasma Process* 15(2):279–307
55. Capitelli M, Colonna G, Gorse C et al (2000) Transport properties of high temperature air in local thermodynamic equilibrium. *Eur Phys J D* 11:279–289
56. D'Angola A, Colonna G, Gorse C et al (2008) Thermodynamic and transport properties in equilibrium air plasmas in a wide pressure and temperature range. *Eur Phys J D* 46:129–150
57. Bailey HE (1967) Programs for computing equilibrium thermodynamic properties of gases. NASA Tech Note NASA-TN-D-3921
58. Cheatwood FM, Gnoffo PA (1996) User's manual for the Langley aerothermodynamic upwind relaxation algorithm (LAURA). NASA Tech Memo NASA-TM-4674
59. Candler GV, Wright MJ, McDonald JD (1994) Data-parallel lower-upper relaxation method for reacting flows. *AIAA J* 32(12):2380–2386
60. Scalabrin LC, Boyd ID (2005) Development of an unstructured Navier-Stokes solver for hypersonic nonequilibrium aerothermodynamics. Paper presented at the 38th AIAA thermophysics conference, Toronto, 6-9 June 2005
61. Nompelis I, Drayna TW, Candler GV (2004) Development of a hybrid unstructured implicit solver for the simulation of reacting flows over complex geometries. Paper presented at the 34th AIAA fluid dynamics conference and exhibit, Portland, 28 June - 1 July 2004
62. Mack A, Hannemann V (2002) Validation of the unstructured DLR-TAU-Code for hypersonic flows. Paper presented at the 32nd AIAA fluid dynamics conference and exhibit, St Louis, 24-26 June 2002
63. Gollan RJ, Jacobs PA (2013) About the formulation, verification and validation of the hypersonic flow solver Eilmer. *Int J Numer Meth Fluids* 73(1):19–57
64. Lani A, Villedieu N, Bensassi K et al (2013) COOLFluid: an open computational platform for multi-physics simulation and research. Paper presented at the 21st AIAA computational fluid dynamics conference, San Diego, 24-27 June 2013
65. Casseau V, Palharini RC, Scanlon TJ et al (2016) A two-temperature open-source CFD model for hypersonic reacting flows, part one: zero-dimensional analysis. *Aerospace* 3(4):34
66. Casseau V, Espinoza DER, Scanlon TJ et al (2016) A two-temperature open-source CFD model for hypersonic reacting flows, part two: multi-dimensional analysis. *Aerospace* 3(4):45
67. Goodwin DG, Moffat HK, Speth RL (2017) Cantera: An object-oriented software toolkit for chemical kinetics, thermodynamics, and transport processes. <http://www.cantera.org>, Version 2.3.0
68. Campoli L, Oblapenko GP, Kustova EV (2019) KAPPA: Kinetic approach to physical processes in atmospheres library in C++. *Comput Phys Commun* 236:244–267
69. Gallis MA, Bond RB, Torczynski JR (2009) A kinetic-theory approach for computing chemical-reaction rates in upper-atmosphere hypersonic flows. *J Chem Phys* 131(12):124311
70. Candler GV, McCormack RW (1991) Computation of weakly ionized hypersonic flows in thermochemical nonequilibrium. *J Thermophys Heat Transf* 5(3):266–273
71. Gnoffo PA, Gupta RN, Shinn JL (1989) Conservation equations and physical models for hypersonic air flows in thermal and chemical nonequilibrium. NASA Tech Publ NASA-TP-2867
72. Park C (1989) Assessment of two-temperature kinetic model for ionizing air. *J Thermophys Heat Transf* 3(3):233–244
73. Moss JN (1974) Reacting viscous-shock-layer solutions with multicomponent diffusion and mass injection. NASA Tech Rept NASA-TR-R-411
74. Blottner FG (1969) Viscous shock layer at the stagnation point with nonequilibrium air chemistry. *AIAA J* 7(12):2281–2288
75. Dunn MG, Kang S (1973) Theoretical and experimental studies of reentry plasmas. NASA Cont Rept NASA-CR-2232
76. Park C (1985) On convergence of computation of chemically reacting flows. Paper presented at the 23rd aerospace sciences meeting, Reno, 14-17 January 1985
77. Park C (1987) Assessment of two-temperature kinetic model for ionizing air. Paper presented at the 22nd thermophysics conference, Honolulu, 8-10 June 1987
78. Park C (1989) A review of reaction rates in high temperature air. Paper presented at the 24th thermophysics conference, Buffalo, 12-14 June 1989
79. Park C, Howe JT, Jaffe RL et al (1991) Chemical-kinetic problems of future NASA missions. Paper presented at the 29th aerospace sciences meeting, Reno, 7-10 January 1991
80. Park C, Jaffe RL, Partridge H (2001) Chemical-kinetic parameters of hyperbolic earth entry. *J Thermophys Heat Transf* 15(1):76–90
81. Ozawa T, Zhong J, Levin DA (2008) Development of kinetic-based energy exchange models for noncontinuum, ionized hypersonic flows. *Phys Fluids* 20(4):046102
82. Bird GA (2011) The Q-K model for gas-phase chemical reaction rates. *Phys Fluids* 23(10):106101
83. Wang XY, Yan C, Zheng YK et al (2017) Assessment of chemical kinetic models on hypersonic flow heat transfer. *Int J Heat Mass Transf* 111:356–366
84. Hao J, Wang J, Lee C (2016) Numerical study of hypersonic flows over reentry configurations with different chemical nonequilibrium models. *Acta Astronaut* 126:1–10

85. Niu Q, Yuan Z, Dong S et al (2018) Assessment of nonequilibrium air-chemistry models on species formation in hypersonic shock layer. *Int J Heat Mass Transf* 127:703–716
86. Capitelli M, Colonna G, Gorse C et al (1996) Thermodynamic properties of high-temperature air components. In: Capitelli M (eds) *Molecular physics and hypersonic flows*. NATO ASI Series, vol 482. Springer, Dordrecht
87. Meher KC, Tiwari N, Ghorui S (2015) Thermodynamic and transport properties of nitrogen plasma under thermal equilibrium and non-equilibrium conditions. *Plasma Chem Plasma Process* 35:605–637
88. Palmer G (1997) An assessment of transport property methodologies for hypersonic flows. Paper presented at the 35th aerospace sciences meeting and exhibit, Reno, 6–9 January 1997
89. Capitelli M, Gorse C, Longo S et al (2000) Collision integrals of high-temperature air species. *J Thermophys Heat Transf* 14(2):259–268
90. Blottner FG, Johnson M, Ellis M (1971) Chemically reacting viscous flow program for multi-component gas mixtures. Sandia Labs Tech Rept SC-RR-70-754
91. Zeng J, Li Q, Wu L (2022) Kinetic modeling of rarefied molecular gas dynamics. *Acta Aerodyn Sin* 40(2):1–30 (in Chinese)
92. Wilke CR (1950) A viscosity equation for gas mixtures. *J Chem Phys* 18(4):517–519
93. Palmer GE, Wright MJ (2003) Comparison of methods to compute high-temperature gas viscosity. *J Thermophys Heat Transf* 17(2):232–239
94. Alkandry H, Boyd ID, Martin A (2013) Comparison of models for mixture transport properties for numerical simulations of ablative heat-shields. Paper presented at the 51st AIAA aerospace sciences meeting including the new horizons forum and aerospace exposition, Grapevine, 7–10 January 2013
95. Armaly BF, Sutton K (1980) Viscosity of multicomponent partially ionized gas mixtures. Paper presented at the 15th thermophysics conference, Snowmass, 14–16 July 1980
96. Alkandry H, Boyd ID, Martin A (2014) Comparison of transport properties models for flowfield simulations of ablative heat shields. *J Thermophys Heat Transf* 28(4):569–582
97. Ramshaw JD, Chang CH (1993) Ambipolar diffusion in two-temperature multicomponent plasmas. *Plasma Chem Plasma Process* 13(3):489–498
98. Sutton K, Gnoffo PA (1998) Multi-component diffusion with application to computational aerothermodynamics. Paper presented at the 7th AIAA/ASME joint thermophysics and heat transfer conference, Albuquerque, 15–18 June 1998
99. Gosse R, Candler G (2005) Diffusion flux modeling: application to direct entry problems. Paper presented at the 43rd AIAA aerospace sciences meeting and exhibit, Reno, 10–13 January 2005
100. Shoen G, Oblapenko G, Kunova O et al (2018) Validation of vibration-dissociation coupling models in hypersonic non-equilibrium separated flows. *Acta Astronaut* 144:147–159
101. Petrov NV, Kirilovskiy SV, Poplavskaya TV et al (2016) A numerical study of non-equilibrium flows with different vibrational relaxation models. *Tech Phys Lett* 42(7):697–700
102. Kustova EV, Oblapenko GP (2016) Mutual effect of vibrational relaxation and chemical reactions in viscous multi-temperature flows. *Phys Rev E* 93(3):033127
103. Schwartz RN, Slawsky ZI, Herzfeld KF (1952) Calculation of vibrational relaxation times in gases. *J Chem Phys* 20(10):1591–1599
104. Capitelli M, Ferreira CM, Gordiets BF et al (2000) Rate coefficients for vibrational relaxation. In: *Plasma kinetics in atmospheric gases*. Springer Series on Atomic, Optical, and Plasma Physics, vol 31. Springer, Berlin, Heidelberg
105. Kustova EV, Oblapenko GP (2015) Reaction and internal energy relaxation rates in viscous thermochemically non-equilibrium gas flows. *Phys Fluids* 27(1):016102
106. Oblapenko GP (2018) Calculation of vibrational relaxation times using a kinetic theory approach. *J Phys Chem A* 122(50):9615–9625
107. Knab O, Frühauf HH, Messerschmid EW (1995) Theory and validation of the physically consistent coupled vibration-chemistry-vibration model. *J Thermophys Heat Transf* 9(2):219–226
108. Park C (1988) Two-temperature interpretation of dissociation rate data for N_2 and O_2 . Paper presented at the 26th aerospace sciences meeting, Reno, 11–14 January 1988
109. Macheret SO, Fridman AA, Adamovich IV et al (1994) Mechanisms of nonequilibrium dissociation of diatomic molecules. Paper presented at the 6th joint thermophysics and heat transfer conference, Colorado Springs, 20–23 June 1994
110. Marrone PV, Treanor CE (1963) Chemical relaxation with preferential dissociation from excited vibrational levels. *Phys Fluids* 6(9):1215–1221
111. Candler GV, Nompelis I (2009) Computational fluid dynamics for atmospheric entry. RTO-AVT-VKI Lecture Series, 2009-AVT-162
112. Josyula E, Bailey WF (2001) Vibration-dissociation coupling using master equations in nonequilibrium hypersonic blunt-body flow. *J Thermophys Heat Transf* 15(2):157–167
113. Hao J, Wang J, Lee C (2017) Assessment of vibration-dissociation coupling models for hypersonic nonequilibrium simulations. *Aerosp Sci Technol* 67:433–442
114. Gökçen T, MacCormack RW (1989) Nonequilibrium effects for hypersonic transitional flows using continuum approach. Paper presented in the 27th aerospace sciences meeting, Reno, 9–12 January 1989
115. Turkyilmazoglu M (2019) Laminar slip wall jet of Glauert type and heat transfer. *Int J Heat Mass Transf* 134:1153–1158
116. Sharipov F (2011) Data on the velocity slip and temperature jump on a gas-solid interface. *J Phys Chem Ref Data* 40(2):023101
117. Maxwell JC (1879) VII. On stresses in rarified gases arising from inequalities of temperature. *Phil Trans R Soc* 170:231–256
118. Wang P, Su W, Wu L (2020) Thermal transpiration in molecular gas. *Phys Fluids* 32(8):082005
119. Greenshields CJ, Reese JM (2012) Rarefied hypersonic flow simulations using the Navier-Stokes equations with non-equilibrium boundary conditions. *Prog Aerosp Sci* 52:80–87

120. Su W, Wang P, Liu H et al (2019) Accurate and efficient computation of the Boltzmann equation for Couette flow: Influence of intermolecular potentials on Knudsen layer function and viscous slip coefficient. *J Comput Phys* 378:573–590
121. Lockerby DA, Reese JM, Gallis MA (2005) Capturing the Knudsen layer in continuum-fluid models of Nonequilibrium gas flows. *AIAA J* 43(6):1391–1393
122. Yang X, Gui Y, Xiao G et al (2020) Reacting gas-surface interaction and heat transfer characteristics for high-enthalpy and hypersonic dissociated carbon dioxide flow. *Int J Heat Mass Transf* 146:118869
123. Scott CD (1992) Wall catalytic recombination and boundary conditions in nonequilibrium hypersonic flows — with applications. In: Bertin JJ, Periaux J, Ballmann J (eds) *Advances in hypersonics*. Progress in scientific computing, vol 8/9. Birkhäuser, Boston
124. Yang Y, Park G (2019) Analysis of catalytic heat transfer for a multi-species gas mixture. *Int J Heat Mass Transf* 137:1088–1102
125. Herdrich G, Fertig M, Petkow D et al (2012) Experimental and numerical techniques to assess catalysis. *Prog Aerosp Sci* 48–49:27–41
126. Yang Y, Kim I, Park G (2019) Experimental and numerical study of oxygen catalytic recombination of SiC-coated material. *Int J Heat Mass Transf* 143:118510
127. Massuti-Ballester B, Pidán S, Herdrich G et al (2015) Recent catalysis measurements at IRS. *Adv Space Res* 56(4):742–765
128. Serpico M, Monti R, Savino R (1998) Heat flux on partially catalytic surfaces in hypersonic flows. *J Spacecr Rockets* 35(1):9–15
129. Viviani A, Pezzella G (2007) Catalytic effects on non-equilibrium aerothermodynamics of a reentry vehicle. Paper presented at the 45th AIAA aerospace sciences meeting and exhibit, Reno, 8–11 January 2007
130. Su S, Shi Y, Liu S et al (2018) Finite-rate surface catalysis effects on aero-heating environment of a reentry capsule. *Acta Aerodyn Sin* 35(5):878–884 (in Chinese)
131. Yang Y, Sethuraman VRP, Kim H et al (2022) Determination of surface catalysis on copper oxide in a shock tube using thermochemical nonequilibrium CFD analysis. *Acta Astronaut* 193:75–89
132. Yuan Z, Huang S, Gao X et al (2016) Effects of surface-catalysis efficiency on aeroheating characteristics in hypersonic flow. *J Aerosp Eng* 30(3):04016086
133. Needels JT, Düzel Ü, Hanquist KM et al (2022) Sensitivity analysis of gas-surface modeling in nonequilibrium flows. Paper presented at the AIAA SciTech 2022 Forum, San Diego, 3–7 January 2022
134. Valentini P, Schwartzentruber TE, Cozmuta I (2009) A mechanism-based finite-rate surface catalysis model for simulating reacting flows. Paper presented at the 41st AIAA thermophysics conference, San Antonio, 22–25 June 2009
135. Deutschmann O, Riedel U, Warnatz J (1995) Modeling of nitrogen and oxygen recombination on partial catalytic surfaces. *J Heat Transfer* 117(2):495–501
136. Fertig M (2015) Finite rate surface catalysis modelling of PM1000 and SiC employing the DLR CFD solver TAU. Paper presented at the 8th European symposium on aerothermodynamics for space vehicles, Lisbon, 2–6 March 2015
137. MacLean M, Marschall J, Driver DM (2011) Finite-rate surface chemistry model, II: Coupling to viscous Navier-Stokes code. Paper presented at the 42nd AIAA thermophysics conference, Honolulu, 27–30 June 2011
138. Marschall J, MacLean M (2011) Finite-rate surface chemistry model, I: Formulation and reaction system examples. Paper presented at the 42nd AIAA thermophysics conference, Honolulu, 27–30 June 2011

Publisher's Note

Springer Nature remains neutral with regard to jurisdictional claims in published maps and institutional affiliations.

Submit your manuscript to a SpringerOpen[®] journal and benefit from:

- Convenient online submission
- Rigorous peer review
- Open access: articles freely available online
- High visibility within the field
- Retaining the copyright to your article

Submit your next manuscript at ► [springeropen.com](https://www.springeropen.com)
